UNIVERSITY OF OSLO
DEPARTMENT OF PHYSICS

MASTER'S THESIS

Quantum Mechanical Modelling and Optical Spectroscopy of Zn(Mg,Cd)O Heterostructures

Marius Mordal Bakke

A thesis submitted in partial fulfilment of the requirements for the degree of MSc

in

Materials, Energy and Nanotechnology

May, 2016

Abstract

In the past 10 years, ZnO as a semiconductor has attracted considerable attention due to its unique properties; such as high electron mobility, wide and direct bandgap, high oscillator strength, and a large exciton binding energy. The increasing interest in ZnO-based electronics can largely be attributed to new promising applications offered by alloying and nanostructuring. Among such novelties are band engineered Zn(Mg,Cd)O compounds with a tunable optical gap from 1.8 eV to 4.8 eV.

The present work investigates the importance of alloy composition, the structuring of Zn(Mg,Cd)O heterostructures, and the related polarization fields and quantum confinement effects, including the quantum confined Stark effect. Optical characterization by photoluminescence spectroscopy and quantum mechanical modelling utilizing $k \cdot p$ perturbation theory is used to provide a better understanding of the underlying mechanisms of said quantum confinement effects and charge carrier dynamics.

To aid heterostructure design and nanostructure modelling, essential material parameters such as band parameters and deformation potentials are required. Following from the lack of available experimental data for wurtzite MgO and CdO, essential material parameters of these, required in $k \cdot p$ perturbation theory treatment of Zn(Mg,Cd)O heterostructures, are found to be poorly defined. Implications and possible solutions to this are discussed in the context of quantum mechanical modelling.

Increased coupling between wells with decreasing barrier height and width in the case of ZnO/$Zn_{1-x}Mg_xO$ multiple quantum well structure is shown. Further evidence is presented showing the dependence of quantum well width in our Zn(Mg,Cd)O heterostructures with regards to quantum confinement effects. It is shown under which conditions the quantum confined Stark effects are expected to take place, and a detailed description of carrier recombination as a function of temperature is presented. En masse, these studies may facilitate the correlation of the performance of ZnO-based heterostructures to their processing, a matter of fundamental interest as Zn(Mg,Cd)O heterostructures and multiple quantum well structures show several promising applications in practical device implementation.

Acknowledgements

The author gratefully acknowledges: The LENS group, Dr. Vishnukanthan Venkatachalapathy for providing MOVPE grown Zn(Mg,Cd)O MQW samples, Dr. Augustinas Galeckas and Prof. Andrej Yu Kuznetsov for critical reviews of the work, and Augustinas Galeckas once again for valuable assistance with PL measurements, coffee breaks and discussions.

Marius Mordal Bakke
May 2016

Nomenclature

In alphabetical order

- 2DEG - Two-Dimensional Electron Gas
- BE - Bound Exciton
- CdO - Cadmium Oxide
- DFT - Density Functional Theory
- DOS - Density of States
- EHP - Electron-Hole Pair
- FE - Free Exciton
- hh - heavy hole
- LA - Longitudinal Acoustic
- LDA - Local Density Approximation
- lh - light hole
- LO - Longitudinal Optical
- MgO - Magnesium Oxide
- MQW - Multiple Quantum Well
- NBE - Near Band Emission
- PL - Photoluminescence
- PLE - Photoluminescence Excitation
- QC - Quantum Confinement
- QW - Quantum Well
- QCSE - Quantum Confined Stark Effect
- SL - Superlattice
- SQW - Single Quantum Well
- TA - Transverse Acoustic
- TO - Transverse Optical
- wz - Wurtzite
- zb - Zincblende
- ZnO - Zinc Oxide

Contents

1 Introduction 1

2 Background 3

2.1 Theoretical Background 3
2.1.1 Crystal Structure 3
2.1.2 Crystal Defects 5
2.1.3 The Reciprocal Lattice and The First Brillouin Zone 7
2.1.4 Probability and The Uncertainty Principle 8
2.1.5 The Schrödinger Wave Equation 9
2.1.6 Particle in a Box - Density of States 10
2.1.7 Tunnelling 12
2.1.8 Bandstructure 14
2.1.9 Spin Interactions 15
2.1.10 Effective Mass 17
2.1.11 Quantum Confinement 18
2.1.12 Heterostructures and Low-Dimensional Semiconductors 20
2.1.13 Multiple Quantum Wells and Superlattices 21
2.1.14 Exciton 22
2.1.15 Recombination 23
2.1.16 Oscillator Strength 26
2.2 Experimental Method 27
2.2.1 Photoluminescence Spectroscopy 27
2.3 Theoretical Method 28
2.3.1 Poisson Equation 29
2.3.2 Strain 30
2.3.3 Single-band Envelope Function Approximation (Effective Mass Approximation) 32
2.3.4 Multi-band $k \cdot p$ Envelope Function Approximation 34
2.3.5 Spurious Solutions 35
2.3.6 Boundary Conditions for the Schrödinger Equation 35

3 Results and discussion 37

3.1 Photoluminescence Spectroscopy 37
3.1.1 Time-Integrated (Steady State) Photoluminescence Spectroscopy 39

3.1.2 Time Resolved Photoluminescence Spectroscopy 42
3.2 Quantum Mechanical Modelling 47
3.2.1 Quantum Confinement Effects of a Quantum Well 47
3.2.2 The Extremes 51
3.2.3 Coupling in MQWs 56

4 Summary and Concluding Remarks 61
4.1 Summary 61
4.2 Concluding Remarks 62
4.3 Future Work and Potential Applications 63

Chapter 1

Introduction

We rely on fossil fuels for more than 80% of our current energy needs, a situation which is not sustainable in the long-term. On top of this, the energy demand is expected to grow by almost half over the next two decades.[1] The amount of energy the earth's surface receives from the sun in one hour is more than the entire world's energy consumption in one year, and it comes without any emission of greenhouse gases; ZnO structures poses as candidates for highly efficient and affordable solar cells. Furthermore will transitioning to a more efficient light source, such as readily available light emitting diodes, noticeably lower the global energy demand. In fact did the Nobel Prize in Physics 2014 go to Isamu Akasaki, Hiroshi Amano, and Shuji Nakamura for their efforts in the invention of efficient blue light-emitting diodes which has enabled bright and energy-saving white light sources; a feat based on the wide bandgap material GaN, which is very similar in many respects to ZnO.

ZnO-based electronics have recieved an increased amount of interest in recent years, only in 2009 there were more than 5000 publications containing ZnO in the title, a number that increases every year. As a direct wide bandgap semiconductor, with E_g $\sim$3.37 eV at room temperature, and a high exciton binding energy compared to GaN(60 meV as opposed to 20 meV), ZnO is a superior candidate for minority-carrier-based devices, such as light emitting diodes, laser diodes, and transparent p-n junctions. Furthermore it offers significant advantages over group III-Nitride materials, which include an availability of large area lattice-mismatched substrates and a lower material cost. [2, 3, 4, 5]

Following from this, new promising applications are offered by alloying and nanostructuring. Nanostructured ZnO materials show remarkable performance in electronics and optics. With reduction in size, novel electrical, mechanical, and optical properties are introduced, which are understood to be the result of surface and quantum confinement effects.[6] Among such novelties are band engineered Zn(Cd,Mg)O compounds with a tunable optical gap from 1.8 eV to 4.8 eV for the use as solar-blind detectors or advanced absorbers of solar radiation in photoelectrochemical and photovoltaic applications. Indeed, the efficiency of sunlight absorption can be increased, e.g by stacking several compositionally graded ZnCdO layers into a multilayer heterostructure, which readily provides broader coverage of solar spectrum and more efficient charge separation due to the built-in field; an equally promising strategy in this respect is to employ Zn(Cd,Mg)O multiple quantum well structures. In spite of certain maturity

of bandgap engineering and significant progress reached in realization of novel functionalities in ZnO-based heterostructures, including LENS' own efforts in fabricating multiple quantum wells, some critical topics in material properties, such as charge carrier transport and its correlation with alloy composition, remain scarcely studied. The particular importance of a systematic knowledge of carrier lifetimes for variable composition compounds arises from the fact that binary constituents have different thermodynamically stable crystalline structures, e,g wurtzite for ZnO and rock-salt for CdO/MgO), while also exhibiting low thermodynamic solubility. Both factors point towards likely deterioration of crystallinity and phase separation for higher (Cd,Mg)-content compounds. Closely related is the polarity issue typical to crystals lacking inversion symmetry, implying non-vanishing spontaneous and piezoelectric polarization fields and electrostatic charge densities in strained Zn(Cd,Mg)O compounds that influence opto-electrical properties and hence device behaviour.

Chapter 2

Background

2.1 Theoretical Background

This section aims to provide and explain the theoretical concepts necessary to fully appreciate the study. It starts out explaining relevant crystal structures and defects, before introducing the idea of the reciprocal lattice. Then a quick introduction to the basic quantum mechanics behind is made, before moving to concepts such as bandstructure, effective mass approximation, heterostructures and confinement, and recombination.

2.1.1 Crystal Structure

A crystalline structure is distinguished by the fact that there is some form of basic arrangement of atoms throughout the solid. This periodicity is defined in terms of a symmetric array of points in space called the lattice. As a consequence of this, the crystal will appear exactly the same at one point as it will at a series of other equivalent points, the distance between which we define as the lattice period. In every case the lattice contains a volume that can be used to represent the entire lattice, we refer to this volume as the *unit cell*. A useful choice of primitive unit cell is the Wigner-Seitz cell, which is defined as the region of space that is closer to one given lattice point than to any other. The possible types of point lattices in three dimensions are limited. By following an arrangement that doesn't restrict the symmetry of our cell, called the *basis*, we can add atoms to lattice points to form 14 different point lattices. We call these the *Bravais lattices*.[7]

The lattice symmetry operations are given as

$$\mathbf{R_n} = n_1\mathbf{a_1} + n_2\mathbf{a_2} + n_3\mathbf{a_3} \tag{2.1}$$

Where n_i are integers and a_i are the primitive vectors that span the lattice. The set of all $\mathbf{R_n}$ form the point lattice of the crystal.

The three types of crystal structures that are of most importance to semiconductors are wurtzite, zincblende and the diamond structure. In the case of ZnO, it can take on two out of these three crystal structures. Under normal conditions the thermodynamically stable phase is wurtzite symmetry, while zincblende structure can be stabilized by growth on cubic substrates. Under strong enough pressures ZnO can also be found in the rocksalt structure.

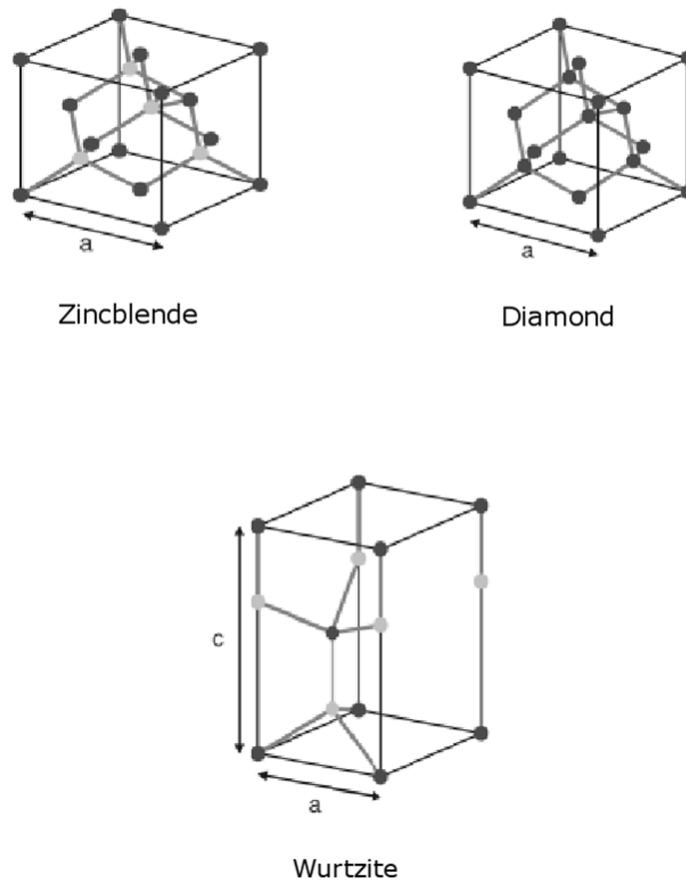

Figure 2.1: Illustration of the three most common semiconductor crystal structures. Zincblende(e.g GaAs), Diamond(e.g Si) and Wurtzite(e.g ZnO). Original figure from [8]

The wurtzite structure has a hexagonal unit cell with two lattice parameters a and c; the ratio of these are typically given as $c/a = \sqrt{8/3}$. This leads to a lack of inversion symmetry. Such structures are termed non-centrosymmetric, and can give rise to piezo- and pyroelectric effects. [2, 8, 9]

2.1.2 Crystal Defects

By convention we use the ideal crystal structures based on the lattice symmetry operations as the reference point. Any deviation from these ideal crystal structures is defined as a defect. Defects are present at any temperature and occur naturally in all crystalline compounds.

We separate different types of structural defects by dimensionality. If the defect is limited to one structural or lattice site and its immediate vicinity, it's called a zero-dimensional defect, or more commonly a point defect. Examples of point defects are substitutional atoms or empty sites termed vacancies. One-dimensional defects include line defects, e.g a row of vacancies inducing a dislocation. Two-dimensional defects include stacking faults and grain boundaries. Interfaces and surfaces may also be viewed as two-dimensional defects. Some typical defects are presented in Fig. 2.2.

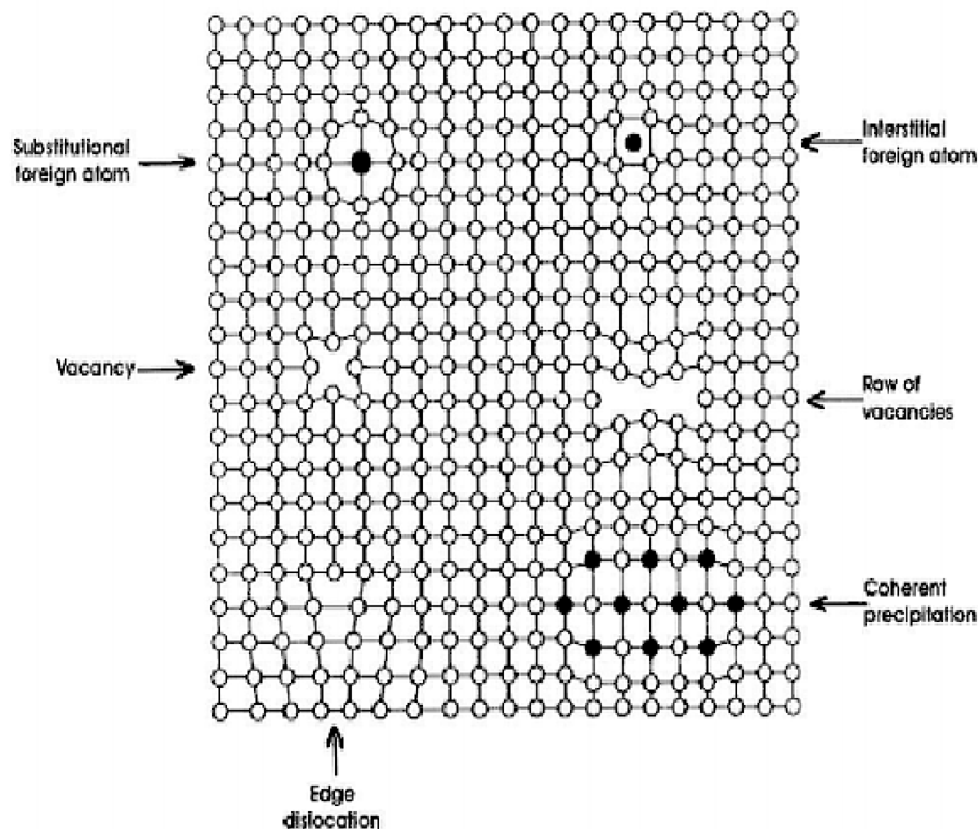

Figure 2.2: Overview of some defects in a crystalline solid. Original figure can be found in[10]

Intentionally introducing defects into our semiconductors to alter their electronic properties can be a very useful tool. One example of this would be to add impurity atoms to our otherwise intrinsic semiconductor, changing the charge carrier concentration. A slightly doped semiconductor is termed *extrinsic*. Semiconductors that have been doped to such extents that they begin to take on metallic properties are called *degenerate*. We separate between n and p doping, the effects of n-doping of an intrinsic semiconductor can be seen in Fig. 2.3. Dopant atoms that give rise to free electrons in the conduction band are called donors, and those that give rise to free holes in the valence band are called acceptors. The binding energy for these carriers can

be viewed as similar to that of the hydrogen atom. In the case of n doping of this system, it follows

$$E_i = \frac{m_e \cdot e^4}{8\epsilon_0^2 \cdot h^2 \cdot n^2}. \tag{2.2}$$

The state i=1 is the most tightly bound state and corresponds to the ionization energy of the impurity. A binding energy equal to zero corresponds to an electron moving freely in the conduction band. When dealing with semiconductors we have to replace the electron mass with the effective electron mass and the dielectric constant corresponding to $\epsilon_0\epsilon_r$.

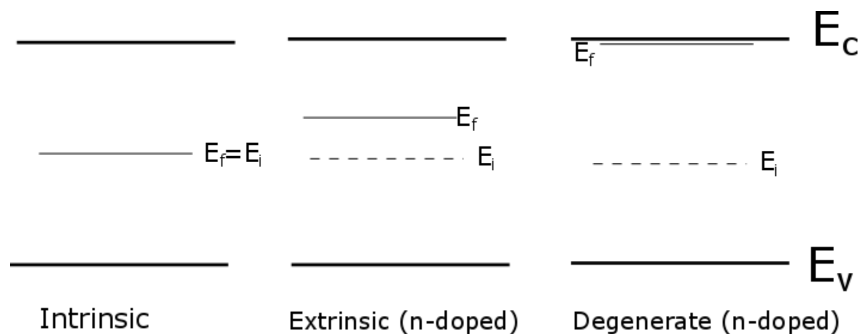

Figure 2.3: Position of the Fermi level in the bandgap with increasing n-doping concentrations

Another way defects are introduced is during growth. We separate between two ways of growing layers on a substrate, termed *homoepitaxy* and *heteroepitaxy*. Growing layers on a substrate with matching lattice constants is called *homoepitaxy*, while the opposite case, growing layers with different lattice constants with respect to the substrate, is called *heteroepitaxy*. By growing thin enough layers, of the order of 10 nm, the heteroepitaxial layers can be grown with a lattice constant in compliance with that of the substrate, but at the same time it induces *strain* to the structure. This type of growth is termed *pseudomorphic*. In the case where the epitaxial layer exceeds some critical layer thickness t_c, the strain energy leads to the formation of defects in the crystal structure. Strain has some very important effects on semiconductors with respect to the electronic structure and polarization charges, both of which will be discussed in later chapters.

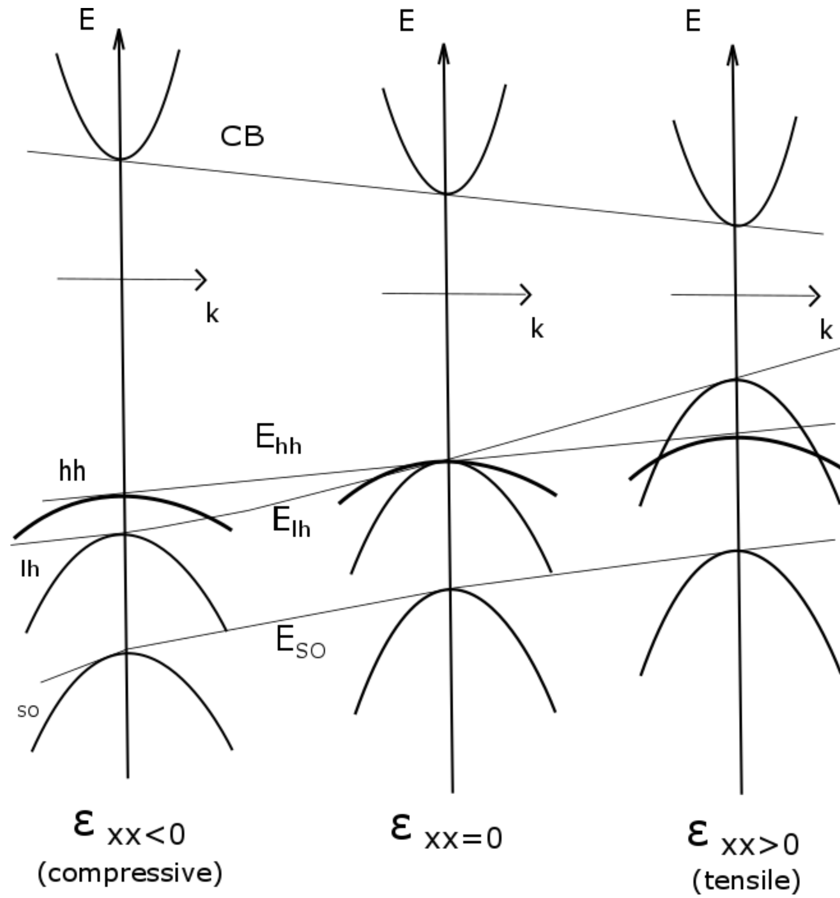

Figure 2.4: Illustration of the effect of varying from compressive strain to tensile strain on the bandstructure of a direct bandgap material

In the case of highly mismatched substrates in ZnO, there is usually a certain amount of zincblende phase of ZnO separated by crystallographic defects from the wurtzite phase.[2, 7, 9, 10, 11]

2.1.3 The Reciprocal Lattice and The First Brillouin Zone

The concept of the reciprocal lattice is fundamental to semiconductor physics as it simplifies the description of periodic structures. We recall that for a given Bravais lattice

$$\mathbf{R_n} = n_1\mathbf{a_1} + n_2\mathbf{a_2} + n_3\mathbf{a_3}.$$

We then define the reciprocal lattice as the set of vectors $\mathbf{G}$ for which

$$\mathbf{R} \cdot \mathbf{G} = 2\pi \cdot l, \tag{2.3}$$

where l is an integer. This can be rewritten on the form

$$e^{(i\mathbf{G}\cdot\mathbf{R})} = 1. \tag{2.4}$$

G may be written as the sum of three vectors

$$\mathbf{G} = n_1\prime\mathbf{b_1} + n_2\prime\mathbf{b_2} + n_3\prime\mathbf{b_3}, \tag{2.5}$$

where $n_1\prime, n_2\prime, n_3\prime$ are integers, and the vectors $\mathbf{b_1}, \mathbf{b_2}, \mathbf{b_3}$ span the reciprocal lattice and are given as

$$\mathbf{b_1} = 2\pi\frac{\mathbf{a_2} \times \mathbf{a_3}}{\mathbf{a_1} \cdot (\mathbf{a_2} \times \mathbf{a_3})}, \mathbf{b_2} = 2\pi\frac{\mathbf{a_3} \times \mathbf{a_1}}{\mathbf{a_1} \cdot (\mathbf{a_2} \times \mathbf{a_3})}, \mathbf{b_3} = 2\pi\frac{\mathbf{a_1} \times \mathbf{a_2}}{\mathbf{a_1} \cdot (\mathbf{a_2} \times \mathbf{a_3})}. \tag{2.6}$$

This gives us the relation

$$\mathbf{a_i} \cdot \mathbf{b_j} = 2\pi\delta_i j, \tag{2.7}$$

Where $\delta = \begin{cases} 1, & \text{if } i = j, \\ 0, & \text{if } i \neq j \end{cases}.$

In one dimension this gives us a reciprocal lattice vector $k = \frac{2\pi}{a}$, which corresponds to the size of the first Brillouin zone. This can be generalized into the three dimensional case of a cubic crystal with lattice spacing *a* in all directions. In this case k turns into a real wave vector **k**

$$\mathbf{k} = (k_x, k_y, k_z) = \frac{2\pi(n_x, n_y, n_z)}{aN} = \frac{2\pi(n_x, n_y, n_z)}{L} \tag{2.8}$$

Where N is the number of atoms, L is the macroscopic side length of our cubic crystal, and n_x, n_y, n_z being integers.

The definition of the first Brillouin zone is the region of reciprocal space, also denoted **k**-space, that is closer to a given reciprocal lattice point than any other. As such we note that it corresponds to the Wigner-Seitz cell in real space. In the first Brillouin zone, including its boundaries, we denote points of high symmetries with capital letters. Γ corresponds to the center of the Brillouin zone where $\mathbf{k} = (0, 0, 0)$, while L and X corresponds to the boundaries. [9]

2.1.4 Probability and The Uncertainty Principle

When dealing with particles on the atomic scale it is impossible to describe, with precision, events including position, momentum and energy. Therefore we speak instead of *expectation values*. The uncertainty ingrained in quantum theory describes the probabilistic nature of events involving these particles. The magnitude of this uncertainty is given by the *Heisenberg uncertainty principle*

$$\delta x \delta p \geq \hbar/2 \tag{2.9}$$

As we can see it is impossible to simultaneously measure precisely position and momentum of the particle; these are called incompatible observables, and are identified by a non-complete set

of shared eigenfunctions. A collapse of the wavefunction upon measurement of one will thus change the properties of the other. A similar relation can be found for energy and time:

$$\delta E \delta t \geq \hbar/2 \tag{2.10}$$

We also have compatible observables where a collapse of the wavefunction will not create any changes, such as position in different directions, x y z, and direction based momentum, p_x, p_y.

The implication of incompatible observables is that we end up speaking of probabilities. One of the important results of quantum mechanics is that we can obtain a *probability density function* for a particle in a given environment. This function can in turn be used to give us the expectation value of important properties, such as the energy and position of the particle. Given a a probability density function $P(x)$, the probability for finding the particle in a range from x to $x + dx$ can be written as

$$\int_{-\infty}^{\infty} P(x)dx = 1 \tag{2.11}$$

[7, 12]

2.1.5 The Schrödinger Wave Equation

Each particle in a physical system is described by a wavefunction $\Psi(\mathbf{r}, t)$ This function and its space derivative are continuous, finite and single valued. Once the wavefunction is found for a particle, it is possible to calculate its average position, momentum, and energy within the limits of the *uncertainty principle*.

The expectation value <M> for any variable M is calculated from the wavefunction by

$$\langle M \rangle = \int_{-\infty}^{\infty} \Psi^* M_{op} \Psi. \tag{2.12}$$

The Shcrödinger equation in three dimensions is given as

$$-\frac{\hbar}{2m}\nabla^2\Psi + V\Psi = -\frac{\hbar}{j}\frac{\partial \Psi}{\partial t}. \tag{2.13}$$

It is normal to separate this further into a time-independent equation(2.14), and solve them separately

$$\widehat{H}\Psi = E\Psi. \tag{2.14}$$

2.1.6 Particle in a Box - Density of States

Distinctive features of semiconductor structures can be illustrated by application of the effective mass approximation. Take the quasi-particle wavefunction in the form of a plane wave

$$\psi(\mathbf{r}) = Ke^{(\mathbf{ik \cdot r})}. \tag{2.15}$$

The product of a wavefunction with its complex conjugate

$$\psi(\mathbf{r})\psi^*(\mathbf{r}) = w(\mathbf{r})dV, \tag{2.16}$$

yields the probability of finding a particle inside a volume $dV = dxdydz$ At the position described by vector $\mathbf{r}$.

Integrating the probability density of the whole system with a volume V_{syst} gives us a normalization condition that allows us to find the value of K in the wavefunction

$$1 = \int_{sys} w(\mathbf{r})dV = K^2 \int_{sys} e^{i\mathbf{k \cdot r}} e^{-i\mathbf{k \cdot r}} dV = K^2 V_{sys} \Rightarrow K = \frac{1}{\sqrt{V_{sys}}}.$$

For an infinite system $V_{sys} \to \infty$ and $K \to 0$. For 3D, 2D and 1D systems with finite volumes, L^3, L^2 and L respectively, K is equal to $L^{-3/2}$, L^{-1} and $L^{-1/2}$.

If we restrict the motion of the quasi-particle along any axis in a box of length L, and set infinite barrier potentials at the walls of the box, the probability of finding the particle outside the box is 0. It follows from this boundary condition that the wavefunction has to be zero at the walls. These conditions are satisfied by standing waves, which are formed by a superposition of waves with inverse wavevectors $\mathbf{k}$ and $-\mathbf{k}$. This means that $|\mathbf{k}| = n(\pi/L)$, where $n = 1, 2, 3....$

This condition holds true for any dimension in which the particle's motion is restricted. Viewing this from $\mathbf{k}$-space, the allowed states are distributed along k_x, k_y, and k_z with a period of π/L. One state thus has to occupy a volume corresponding to $(\pi/L)^d$, where d stands for the dimension in space.

It is now possible to calculate the density of states in $\mathbf{k}$-space as the number of available states whose wavevector modulus $|\mathbf{k}| = k$ falls within the interval $(k + dk)$. Thus it is necessary to count the number of states within the segments $(k, k+dk)$ and $(-k, -(k+dk))$, and the density of states is given as:

$$\rho(k)dk = g_s dV_k \frac{1}{(\pi/L)^d} \tag{2.17}$$

Where g_s is the degeneracy factor, equal to 2 for fermions, and gV_k is the volume in $\mathbf{k}$-space in which k_x, k_y, and k_z are positive whilst their amplitude k lies within the range of $(k, k + dk)$.

For $d = 2$ the density of states reads

$$\rho(k)dk = g_s dV_k \frac{L^2}{(2\pi)} kdk. \tag{2.18}$$

It is now also possible to write out the density of states in energy space, $\rho(E)$ This gives us the number of states per unit volume and per unit energy.

$$\rho(E)dE = \rho(k(E))\frac{dk}{dE}dE \tag{2.19}$$

For the isotropic case, and

$$\rho(E)dE = \rho(k(E))\frac{q}{|grad_k E(\mathbf{k})|}dE, \tag{2.20}$$

which is the general expression valid for all cases. In the simple case of an electron in a parabolic shape conduction band

$$E(k_c) = E_g + \frac{\hbar^2 k_e^2}{2m_c},$$

giving us

$$k = \frac{\sqrt{2m_c}}{\hbar} \cdot \sqrt{E - E_g}, \frac{dk}{dE} = \frac{\sqrt{2m_c}}{2\hbar} \cdot \frac{1}{\sqrt{E - E_g}}. \tag{2.21}$$

Substituting 2.20 and 2.18 into 2.19 we find for $d = 2$

$$\rho(E) = g_s \frac{m}{2\pi\hbar^2}. \tag{2.22}$$

The plot of density of states versus energy space for different dimensions can be found in figure 2.5.[12, 13, 14]

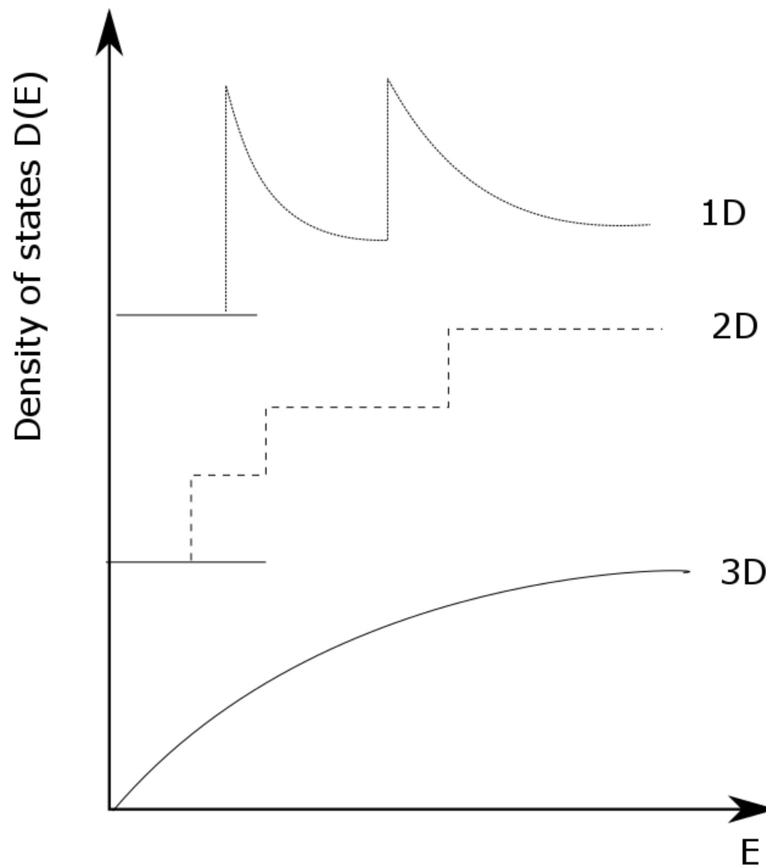

Figure 2.5: Density of states in the conduction band in the case of 3, 2 and 1 dimensional structures

2.1.7 Tunnelling

In the classical problem of a particle in a well, when dealing with infinite barriers, the wavefunction goes to 0 at the boundaries. If however these barriers are non-infinite, the wavefunction is no longer forced to go to 0 at the barrier boundary, and may also be non-zero beyond it. We note that since ψ has a value beyond the barrier there is a chance of finding our quantum particle outside of the well, i.e the particle has penetrated the barrier. This mechanism is called *tunnelling*, and is closely related to the uncertainty principle, meaning that if the barrier is thin enough it is impossible to say with certainty that the particle exists on only one side of it. The

probability density decreases rapidly inside the barrier, so by increasing the barrier width it is possible to decrease tunnelling to a negligible amount. [12, 7]

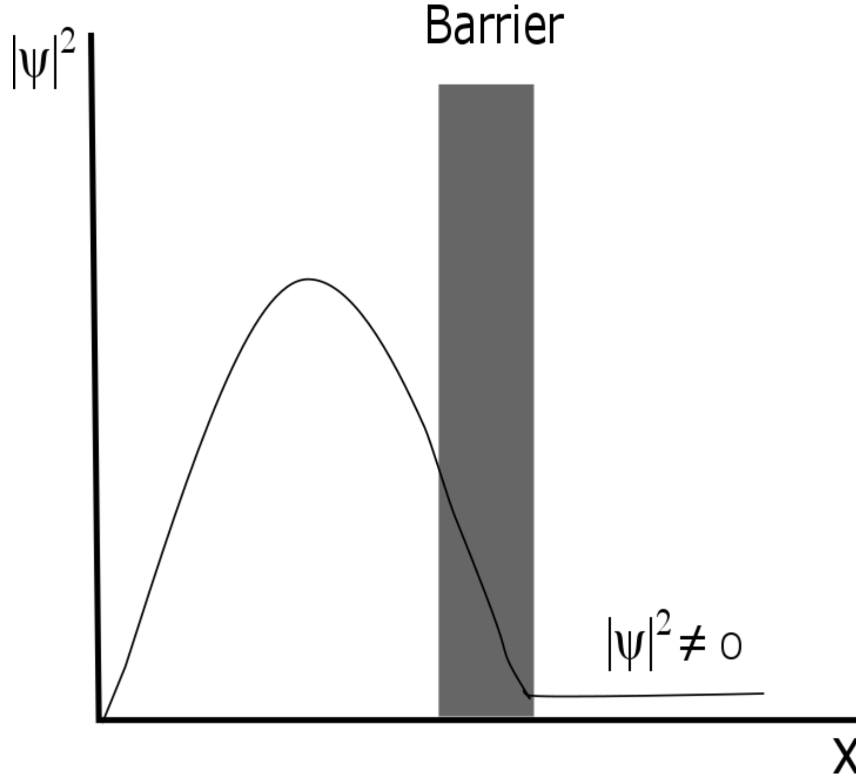

Figure 2.6: Tunneling of a quantum particle through a barrier of width W. The wavefunction drops exponentially inside barrier, but is still non-zero on the other side.

It is possible to show that tunnelling is also dependent on barrier height. The idea of quantum tunnelling is closely related to the uncertainty principle, and we may view this in the context of position-momentum uncertainty. We recall from section 2.4

$$\delta x \delta p \geq \hbar/2.$$

The probability of finding a particle tunneling through the barrier in our figure, corresponding to $x_0 + b$, is proportional to

$$\propto exp[-\frac{2}{\hbar}\int_{x_0}^{x_0+b}\sqrt{2m(V(x)-E)}dx]. \tag{2.23}$$

For a non-negligible probability, it is further required

$$2\sqrt{2m(V_m - E)}b \approx \hbar, \tag{2.24}$$

where V_m is the maximum height of the barrier potential. Measuring the particle coordinate with accuracy $\delta x < b$ yields

$$\delta p^2 = \frac{\hbar^2}{4(\delta x)^2} = \frac{\hbar^2}{4b^2}. \tag{2.25}$$

Combining 2.24 and 2.25, we get

$$\frac{\delta p^2}{2m} = V_m - E. \tag{2.26}$$

Meaning the kinetic energy of the particle, $\frac{p^2}{2m}$, must be greater than the difference between the height of the barrier, V_m, and the total energy E, for it to tunnel through the barrier.[15]

2.1.8 Bandstructure

There are two main approaches to the problem of band structure calculations. In one case we start with free electrons, which have the parabolic energy dispersion

$$E(\mathbf{k}) = \frac{\mathbf{p^2}}{2m_0} = \frac{\hbar^2\mathbf{k}^2}{2m_0}. \tag{2.27}$$

The potential energy of an electron in a crystal is periodic in space. As a consequence of this, the energy spectrum consists of allowed and forbidden energy bands. The electron states can be characterized by its quasimomentum, also known as crystal momentum, $\mathbf{p}$. The quasimomentum is relatable to the more commonly used quasi wavevector by $\mathbf{k} = \mathbf{p}/\hbar$. We shall henceforth be using $\mathbf{k}$ when talking about the bandstructure of semiconductors. The energy in an allowed band is a periodic function of $\mathbf{k}$, so we only have to consider it in the first Brillouin zone. The electron eigenstates of a periodic potential are so-called Bloch waves:

$$\phi_{k,i}(\mathbf{r}) = e^{i\mathbf{kr}} u_{k,i}(\mathbf{r}), \tag{2.28}$$

where

$$u_{k,i}(\mathbf{r}) = u_{k,i}(\mathbf{r} + \mathbf{R}). \tag{2.29}$$

The $\phi_{k,i}(\mathbf{r})$ is a product of a plane wave and a lattice periodic term $u_{k,i}$ where $\mathbf{k}$ is the wave vector and i the index of the band. The eigenenergies in the bands depend on both $\mathbf{k}$ and i and are periodic in the reciprocal space

$$E_i(\mathbf{k}) = E_i(\mathbf{k} + \mathbf{G}). \tag{2.30}$$

Which once again allows the dispersion relation to be reduced to the first Brillouin zone. The allowed number of states is twice the number of elementary cells in the crystal, the doubling is due to spin. And so the energy spectrum for all the allowed bands is given by the dependence of energy on $\mathbf{k}$, $E(\mathbf{k})$. In intrinsic semiconductors at 0K temperature, a certain number of the lowest allowed bands are filled up with electrons according to the Pauli exclusion principle, while the higher bands are empty. In general, the upper filled and the lowest empty bands, valence and conduction band respectively, are of interest to us. These bands are separated by a forbidden energy gap denoted E_g.[14, 16]

2.1.9 Spin Interactions

If we construct the wave function for a system of identical particles so that it reflects the requirement that particles are indistinguishable from each other. This means that interchanging particles occupying any pair of states do not change the probability density ($|\Psi|^2$) of the system. This divides all particles in nature into two classes, bosons and fermions.

An example for two non-interacting identical particles will illustrate the point. The probability density of the the two particle wave function $\Psi(\mathbf{r_1}, \mathbf{r_2})$ must be identical to that of the the wave function $\Psi(\mathbf{r_2}, \mathbf{r_1})$ where the particles have been interchanged.

$$|\Psi(\mathbf{r}_1, \mathbf{r}_2)|^2 = |\Psi(\mathbf{r}_2, \mathbf{r}_1)|^2 \tag{2.31}$$

This is achievable in two cases, the symmetric and anti-symmetric:

$$\text{Symmetric case : } \quad \Psi(\mathbf{r}_1, \mathbf{r}_2) = \Psi(\mathbf{r}_2, \mathbf{r}_1)$$

$$\text{Anti-symmetric case : } \quad \Psi(\mathbf{r}_1, \mathbf{r}_2) = -\Psi(\mathbf{r}_2, \mathbf{r}_1)$$

Particles with symmetric wavefunctions under the said particle interchange have integer or zero spin, $0, 1, 2...$, and are termed bosons. Particles with anti-symmetric wave functions under the particle interchange have half-integral intrinsic spin $1/2, 3/2...$ and are called fermions.

Electrons have a spin part, $s = 1/2$, and an associated magnetic moment of the electron $\mu = e\hbar/2mc$. Electron spins can be either parallel or anti-parallel. The existence of this spin, and the associated magnetic moment, has several consequences when dealing with semiconductor systems, some of which are discussed below. [12]

Pauli Exclusion Principle

The Pauli Principle tells us that no two fermions, particles with spin $s = 1/2$, can occupy the same quantum state at the same time. This principle has an effect on the atomic structure, as well as the chemical and physical properties of semiconductor physics.

Exchange Interaction

As previously noted, electron spins can be either parallel or anti-parallel. If the electron spins are parallel, the coordinate part of the wave function should be antisymmetric: $\psi \uparrow\uparrow (r_2, r_1) = -\psi \uparrow\uparrow (r_1, r_2)$ which tells us that the probability of two electrons being very close to each other is small compared to the opposite case, when the spins are anti-parallel; accordingly their coordinate wave function is symmetric: $\psi \uparrow\downarrow (r_2, r_1) = \psi \uparrow\downarrow (r_1, r_2)$. Electrons with parallel spins are better separated in space, so that their mutual repulsion is less, and consequently the energy of the electrostatic interaction for parallel spins is lower.

Exchange interaction is in fact the result of the electrostatic Coulomb interaction between electrons, which becomes spin-dependent due to the wave function requirement of fermions. The exchange interaction is responsible for ferromagnetism. This is generally only of importance for magnetic semiconductors, and for cases where we have semiconductor-ferromagnet interfaces.[12, 16]

Spin-Orbit Interaction

If an observer moves with a velocity v in an external electric field E, he will see a magnetic field $B = (1/c)E \times v$, where c is the velocity of light. This magnetic field acts on the electron magnetic moment $\mu = e\hbar/2mc$, and is the physical origin of the spin–orbit interaction. Due to the spin–orbit interaction, any electric field will act on the spin of a moving electron. It is also responsible for spin relaxation, this can generally be understood as a result of fluctuations in time magnetic fields. In most cases these are effective magnetic fields originating from the spin–orbit or exchange interactions. The spin-orbit interaction essentially changes the valence band energy spectra.[16]

Energy Bands, Light and Heavy Holes

The allowed energy bands in crystals may be thought of as originating from discrete atomic energy levels. These levels are split to form a band when isolated atoms come close enough to each other. Atomic energy levels are generally degenerate, i.e there are several states of the same energy. The degeneracy of these levels can be of consequence to the band energy spectrum of a crystal.

When including spin-orbit interaction, the total orbital and spin angular momenta coupling $(\mathbf{L} - \mathbf{S})$ is broken due to an additional energy proportional to $\mathbf{LS}$, and only the total angular momentum $\mathbf{J} = \mathbf{L} + \mathbf{S}$ is conserved. The eigenvalues of $\mathbf{J}^2$ are $h(j+1)$ with $|l - s| \geq j \geq l + s$, where l is the atomic orbital angular momentum, and s is the spin. Thus the state with $l = 0$, from which the conduction band is built, is not affected with $(j = s = 1/2)$, while the state with $l = 1$, from which the valence band is built, is split into two states with $j = 3/2$ and $j = 1/2$.

The symmetry properties of band states at $k = 0$ are completely similar to those of the corresponding atomic states. Thus for $k = 0$ we must have a four-fold degenerate state $(j = 3/2, \mathbf{J_z} = \pm 3/2, \pm 1/2$ which is separated by an energy distance Δ, the spin–orbit splitting, from a doubly degenerate state $j = 1/2, \mathbf{J_z} = \pm 1/2)$. The conduction band remains doubly degenerate. The value of Δ is small for materials with light atoms, and may be comparable to the bandgap in semiconductors composed of heavy atoms.

The terms "heavy" and "light" originate from the distinct curvatures of the energy dispersions for these bands. For non-zero values of $\mathbf{k}$, the states can no longer be classified as heavy, light and split-off holes.

In the valence band, the spin of light and heavy holes is tightly bound to their momentum, and thus we remember the relation $\mathbf{k} = \mathbf{p}/\hbar$. This leads to some interesting consequences. If there are external forces present, the light and heavy hole states generally become mixed. This could be due to the reflection from an interface, or the introduction of a quantum well structure.[16]

2.1.10 Effective Mass

One important property of semiconductors is that the number of free carriers is relatively small compared to the total number of atoms. Carriers can be produced in our structure either by excitation or by doping. The carrier concentration never exceeds $10^{20}/cm^3$, while the number of $states/cm^3$ in a given energy band is of the order 10^{22}. This means that carriers only occupy a small fraction of the band extrema. As a consequence of this we are mostly interested in the properties of the energy spectrum in the near vicinity of the minimum of the function $E(k)$ for the conduction band, and its maximum for the valence band.

If these extrema correspond to the center of the Brillouin zone, $\mathbf{k} = 0$, which is often referred to as the Γ point, as is the case for ZnO and other materials of interest, then the function $E(\mathbf{k})$ should be parabolic for values close to the Γ point.

$$E_c = \frac{p^2}{2m_c} \tag{2.32}$$

$$E_v = \frac{-p^2}{2m_v} \tag{2.33}$$

Where m_c is the effective mass of electrons and m_v is the effective mass of holes. The extrema of $E(\mathbf{k})$ do not necessarily occur at the center of the Brillouin zone. It is also possible that the effective mass is anisotropic, i.e it varies with different directions in the crystal.

The effective masses do more than describe the curvature of the $E(\mathbf{k})$ parabolic dependence in the vicinity of its maximum or minimum. It can also help tell us what happens to carriers under external forces. This can be the case because of e.g crystal deformation, built-in fields etc.

If we have small carrier energies compared to E_g, and slow spatial variation of the external forces compared to the periodic crystal potential, we can consider our carriers as free particles moving in the external field. The only difference being that they now have an effective mass, and not the free electron mass. This means that the classical motion of a conduction electron in an electric field $\mathbf{E}$ and magnetic field $\mathbf{B}$ is described by Newton's law:

$$m_c \frac{d^2 r}{dt^2} = -e\mathbf{E} - \frac{e}{c} \cdot \mathbf{v} \times \mathbf{B} \tag{2.34}$$

alternatively

$$F = Q(\mathbf{E} + \mathbf{v} \times \mathbf{B}) \tag{2.35}$$

Likewise, if quantum treatment is needed, one may use the Schrödinger equation for an electron in the external field with its effective mass. Once again neglecting the existence of the crystal periodic potential.[16]

2.1.11 Quantum Confinement

Low-dimensional semiconductors separate themselves from bulk structures in more ways than one. Bulk structures can be viewed as homogeneous materials substantially larger than the exciton Bohr radius in all directions. As a result of this the physical effects and electronic states are said to be determined by their chemical composition.

The de Broglie wavelength is the wavelength λ associated with a particle and its momentum p through the Planck constant h, $\lambda = h/p$. In general the de Broglie wavelengths for electrons and holes, λ_e and λ_h, and the Wannier exciton Bohr radius, a_x, are larger than the lattice constant. This means that it is possible to decrease the crystal size so that it is equal to or less than a_x. If this is the case, the electron states are no longer chemically determined, but rather dependent on crystal size. This gives rise to quantum confinement effects.

The principle of quantum confinement lies in the quantization of the kinetic energy, E_k, of a quasi-particle whose motion is restricted to a region comparable to its de Broglie wavelength.

As a result of electronic states being dependent on size rather than just chemical composition, low-dimensional semiconductor structures can be fabricated with properties tailored to specific applications. This is known as band engineering. [13]

Quantum well

Since quantum wells are the focus of this thesis, we will further delve into the quantum confinement effects for these structures.

As previously mentioned, a quantum well can introduce splitting of light and heavy hole bands, blue shifting the absorption band with decreasing well width. In bulk structures the light and heavy holes are often degenerate at the Γ point. In quantum wells the confinement potential lifts this degeneracy as a result of symmetry breaking, and thus the heavy and the light hole bands split. This is illustrated in Fig. 2.7(b).

The quantum confinement effects stemming from the reduction of size in one dimesion can often be viewed in the light of photoluminescence spectroscopy. In the case of quantum wells we often only observe a single emission band, corresponding to the lowest transition. This is a result of the efficient relaxation of higher excited states into the lowest state, from which the radiative recombination takes place. The photoluminescence peak generally undergoes a Stokes shift, i.e it is redshifted compared to the absorption spectra. This is mainly due to energy relaxation within an inhomogeneously broadened band, often due to interface roughness. Another reason for the Stokes shift can be phonon interaction, which will be discussed in section 2.1.15. The

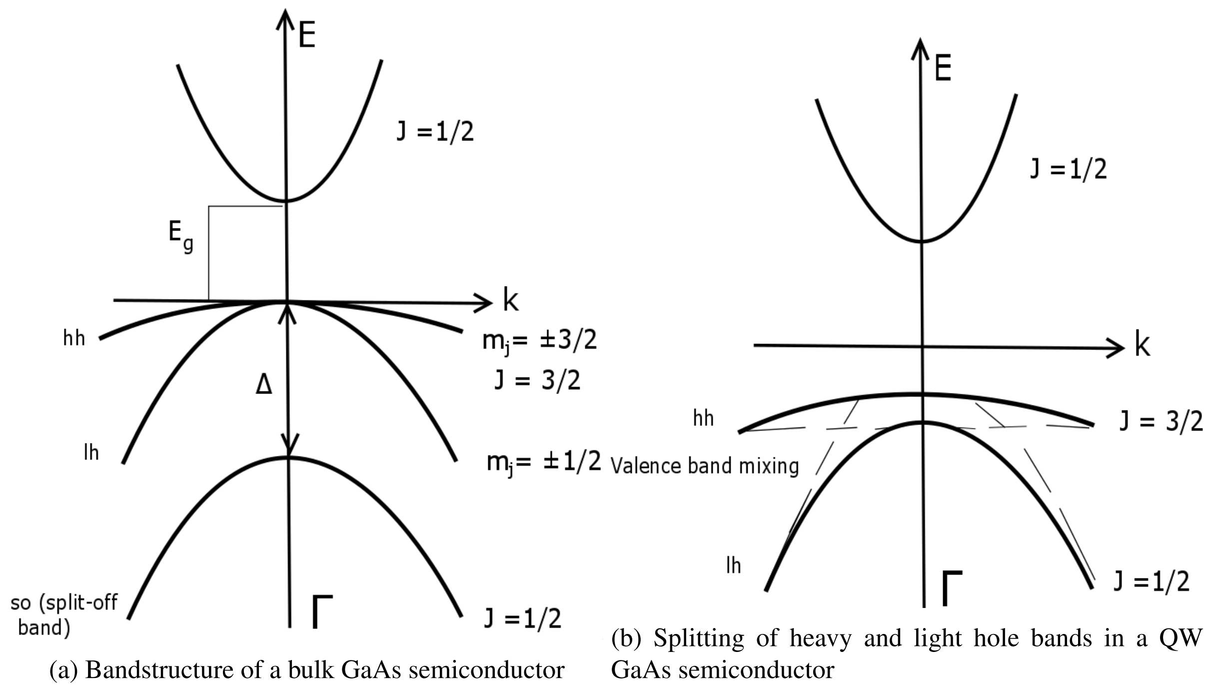

(a) Bandstructure of a bulk GaAs semiconductor

(b) Splitting of heavy and light hole bands in a QW GaAs semiconductor

Figure 2.7: The different bandstructures of a bulk and QW GaAs semiconductor

width of a quantum well is, in practice, not perfectly constant, but it rather has a distribution. The local quantum confinement effects vary accordingly, and gives a smearing of the energy levels. This smearing increases with the number of quantum wells in our heterostructure. The width of photoluminescence bands can be used as a tool for characterizing the quality of our heterostructure.

The most important luminescence properties of free exction recombination in a quantum well can be summarized

- Wavelength(λ) depends on L_W, λ of excitonic luminescence depends on the width of the quantum well. Emission shifts to shorter wavelengths (higher energies) with decreasing well size.
- Luminescence peak from free exciton is expected to be narrower than that of bulk structures, as a result of the difference in the density of states.
- Excitonic binding energies generally increase with decreasing well width, making excitonic phenomena observable at higher temperatures than for bulk structures.
- Nonlinear optical phenomena takes place for lower excitation power densities. Confinement makes it so that excited electron-hole pairs (EHP) cannot travel freely in the crystal, as a result the effective population density can reach high values.

There is always some form of localization of excitons in quantum well structures, so the already mentioned free excitons(Wannier excitons), are never completely delocalized. Local fluctuations in well width and chemical composition variation in our heterostructures does inevitably exist, especially with ternary and quaternary alloys. The wells might also have impurity atoms serving as localization traps for excitons. Due to the smaller amount of material in quantum wells compared to bulk structure, localization centres play a far more important role for optical properties in quantum wells. The observed excitonic emission band should be considered as inhomogeneously broadened due to the superposition of the radiative recombination of free and localized excitons.[13]

2.1.12 Heterostructures and Low-Dimensional Semiconductors

Low-dimensional semiconductor device applications often combine several types of materials, as in the case of the Zn(Mg,Cd)O compounds. There are several reasons for doing this:

- Passivation and protection of nanostructured surface by another material, e.g barrier.
- Embedding of nanostructure into macrostructure, making it easier to manipulate.
- Necessity to fabricate certain energy structures.

These compound structures are called heterostructures. The layered variable bandgap semiconductor heterostructure is formed when a well of lower E_g is surrounded by a higher E_g material serving as a potential barrier.

When we construct heterostructures from materials with different crystal structures, strain is introduced into our sample. This can, as previously discussed, in turn be used to change the bandstructure of our semiconductor.

If one introduce several quantum wells into the heterostructure, and the barrier potential or width is low enough, wavefunctions from other wells can start overlapping, and tunneling between wells become possible. Given that the wavefunction overlap is big enough to form subbands,

we get what is known as a superlattice. A superlattice introduces a new bandstructure and transport properties to the semiconductor.

It is normal to differentiate between different types of quantum wells. These all depend on the band offset, which can be defined by Anderson's rule.[13]

$$\delta E_c = \chi^A - \chi^B$$

$$\delta E_v = \delta E_g - \delta E_c$$

$$Q = \delta E_c / \delta E_v$$

It should be noted that this is the ideal case, and that it often is more complicated in actual heterostructures.

- Type I QW: $E_c(min)$ and $E_v(max)$ in the same layer.
- Type II QW: Extrema found in neighbouring layers. These are misaligned in real space and not in k-space, electrons and holes are spatially separated. Can resemble indirect bandgap material.
- Type III QW: Extremes overlap between neighbouring layers. These layers may freely exchange carriers until equilibrium is reached due to local fields. Resembles a p-n junction.

Low-dimensional semiconductors can be divided into groups according to the number of dimensions in which the structure is restricted to a size small enough to fit the quantum confinement regime. Structures that are not confined in any direction are known as bulk structures. Those that are restricted in one, two or three directions are, respectively, known as quantum wells, quantum wires, and quantum dots.

2.1.13 Multiple Quantum Wells and Superlattices

When dealing with a type I quantum well, the band discontinuities of the conduction and the valence band are such that electrons and holes are confined to the same material. By introducing several quantum wells into a heterostructure, and the barriers between them are sufficiently thick, so that the first quantized electron states of adjacent wells do not overlap, we speak of a multiple quantum well. The density of states increases with the number of identical quantum wells in the structure.

If the barriers in the type I quantum well starts getting thinner and thinner, we enter a regime where the tails of the wavefunctions in the barriers start to overlap. When only dealing with a couple of quantum wells, e.g two, we say that the quantum wells are coupled. If they are identical, the ground state splits into a symmetric and an anti-symmetric part.

By coupling multiple quantum wells along the z-direction, a new periodicity $d = l_z + l_b$ occurs and we obtain a structure known as a one dimensional superlattice.

We recall from section 2.1.3 that we along one dimension have a first Brillouin zone of periodicity $2\pi/a$, as such we can obtain the k_z direction of a Brillouin zone extending from

$$-\frac{\pi}{d} \leq k_z \leq \frac{\pi}{d} \tag{2.36}$$

which is much smaller than the extension in the k_x and the k_y directions. We find a series of minibands in the k_z direction. The difference between a multiple quantum well and a superlattice can be shown in their density of states distribution as a function of energy, as in Fig. 2.8.[14, 13]

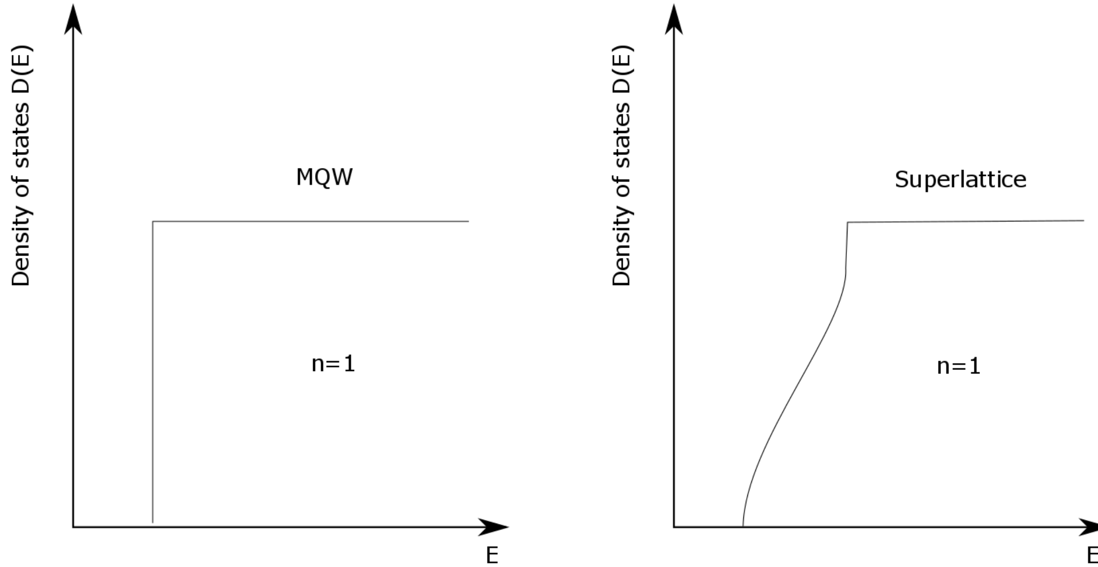

(a) Quantum well in a multiple quantum well structure

(b) Quantum well in a superlattice

Figure 2.8: Density of states as a function of energy of a quantum well in (a) multiple quantum well structure, and (b) superlattice.

2.1.14 Exciton

An exciton in a semiconductor is a bound state of an electron and a hole. It can be viewed as a hydrogen-like system with properties much like that of an electron bound to a donor impurity. An important distinction is that excitons can move inside the crystal. They are also unlikely to exist in an equilibrium state, but are often created by optical excitation and have a lifetime with respect to recombination. In an ideal semiconductor the primary electronic excitation would be that of a free electron-hole pair with a required energy $E \geq E_g$. Electrons and holes are however attracted to each other by Coulomb forces, and an exciton's internal energy is therefore lower

than E_g. The Exciton now represents the lowest electronic excitation in a semiconductor, and it can be observed as an absorption/PL line slightly below the bandgap.

We generally divide excitons into three basic types:

- Frenkel exciton, a small-radius exciton. They occur in molecular crystals.
- Charge transfer exciton. Occurs primarily in ionic crystals.
- Wannier exciton, a large-radius exciton. They occur mainly in semiconductors.

As we can see Wannier excitons are what we are dealing with when it comes to semiconductors. In the case of these, the electron and hole is separated over several lattice constants, and as a result the exciton wave function is strongly delocalized and the exciton can, as previously noted, move freely inside the crystal. [13, 16]

2.1.15 Recombination

Recombination processes between electrons and holes in semiconductor devices can be of both a radiative and a non-radiative nature. As a carrier is excited, it leaves the semiconductor in a non-equilibrium thermodynamic state. After a certain relaxation time it loses its energy and goes back into the ground state. This transition can happen in a number of ways: If the excitation energy is radiated away in the form of a photon we say that the recombination was radiative. Another way is for the excess energy to be transmitted in the form of heat to the lattice, it might induce a photochemical change to the crystal matrix or even generate a lattice defect. These transitions are of the type non-radiative recombination. [13]

Direct Bandgap

Semiconductors mainly fall into two groups: Those with direct bandgap behaviour and those with indirect bandgap behaviour. Some materials, like Ge and CdO, show both. The minimum energy state in the conduction band and the maximum energy state in the valence band are both characterized by the wavevector, $\mathbf{k}$. If the k-vectors, are the same for both extremes, then the respective holes and electrons share the same wavevector and we have a direct bandgap.[7, 13]

A direct bandgap can best be illustrated, in Fig. 2.9, as the ideal case of recombination of a free electron-hole pair, often referred to as band-to-band emission.

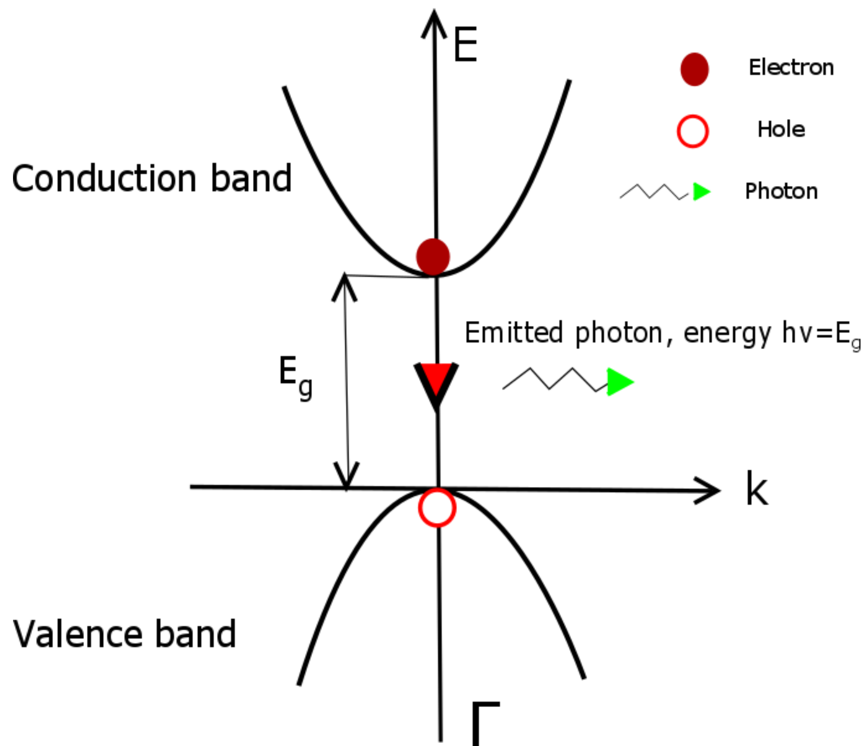

Figure 2.9: Simplified illustration of band to band emission in a direct bandgap

Indirect Bandgap

Now if the wavevectors are not the same for both extremes, we are dealing with an indirect bandgap. The fundamental difference between recombination in the direct and the indirect bandgap lies as noted in the wavevector, **k**, of the holes and the electrons. In a direct bandgap semiconductor we remember that the recombination takes place between holes and electrons of the same wavevector, whereas in an indirect bandgap semiconductor an excited electron of energy E_2 can recombine with any hole of energy E_1 and varying **k**. That is as long as the conservation rule $E_2 - E_1 = hv \pm \hbar\omega$ is fulfilled. The energy $\hbar\omega$ denotes the phonon energy, which takes part in conserving the quasimomentum, here in the case of the quasi wavevector, $\mathbf{k}_{\hbar}\omega = |\mathbf{k}(E_2) - \mathbf{k}(E_1)|$.[13] A simplified illustration of recombination in an indirect bandgap is shown in Fig. 2.10.

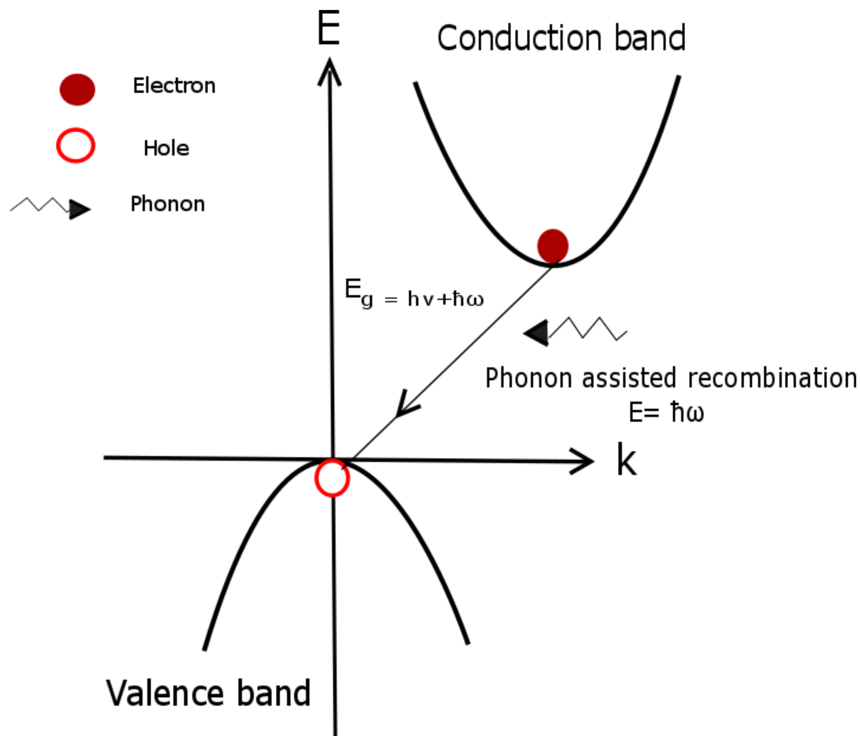

Figure 2.10: Simplified illustration of recombination of electron and hole in the indirect bandgap. The recombination is photon assisted

Radiative Recombination

In our semiconductor system, there are several radiative recombination processes that may occur at the same time[13]:

- Exciton recombination which includes
  - Radiative recombination of free exciton (FE)
  - Radiative recombination of FE with simultaneous emission of LO phonon (FE-LO)
  - Radiative recombination of bound exciton(BE)
    - Exciton bound to neutral/ionized donor
    - Exciton bound to neutral/ionized acceptor
- Radiative recombination of donor-acceptor pairs
- Radiative recombination of free hole with neutral donor or free electron with neutral acceptor
- Radiative recombination with free electron-hole pairs (band-to-band emission)

In the present study we mainly focus on excitonic radiative recombination processes.

Non-Radiative Recombination

The quantum efficiency(QE) is the ratio of photons absorbed to photons emitted through luminescence. This efficiency almost never reaches $\eta = 1$. Furthermore, Stokes law states that the energy of the luminescence photons is less than the energy of the photons of the exciting light, meaning that a portion of the excitation energy is not transformed into luminescence radiation, but rather changed into other types of energy during relaxation to the system ground state.

Depending on the final form of the dissipated excitation energy, one recognize three different types of non-radiative recombination processes in semiconductors:

- Recombination when the energy transforms into heat via lattice vibrations (phonons)
- Recombination leading to the creation of new point defects in the lattice
- Recombination transforming the excitation energy into photochemical changes of the material

The most common non-radiative recombination process is the transformation of excitation energy into lattice heat. The creation of new point defects due to supplied excitation energy is a rare happenstance. Photochemical changes to the material is limited to a few compounds, and not of concern to the case of ii-vi semiconductors.

There are two cases of non-radiative recombination that also should be mentioned, Auger and bimolecular recombination.

Auger and bimolecular recombination

When an incident high-energy electron ejects another electron from an atomic core level, and some electron from an outer shell then falls into the created vacancy, a photon may be emitted or the excitation energy can be handed over to another electron from the same outer shell, ejecting it out from the atom. This ejection of particle is called non-radiative Auger recombination, and even though the ultimate result is a transfer of the kinetic energy into lattice heat, it is sometimes classified as an independent category of non-radiative transitions.

Bimolecular recombination is highly dependent on carrier concentrations, the probability of non-radiative bimolecular recombination in a pure ideal semiconductor is in fact 0. An example of this recombination mechanism could be non-radiative recombination via a trap site in the bandgap, which accepts both electrons and holes. [13]

2.1.16 Oscillator Strength

The optical properties of matter are determined by the coupling of various types of oscillators in matter to the electromagnetic radiation field, i.e an incident electromagnetic field will cause said oscillators to perform driven oscillations. The amplitude of these oscillations depends on the angular frequency ω of the incident field, on the eigenfrequency ω_0 of the oscillators, on

the coupling strength f between the electromagnetic field and oscillator, and on its damping γ.

These properties go together to describe the dielectric function

$$\epsilon(\omega) = 1 + \frac{Ne^2}{\epsilon_0 m}(\omega_0^2 - \omega^2 - i\omega\gamma)^{-1}, \tag{2.37}$$

where N is the number of oscillators per unit volume and ϵ_0 is the dielectric constant.

The term $\frac{Ne^2}{m}$ gives us the coupling strength of the electromagnetic field to the oscillators. In a quantum mechanical model, this coupling is given by the transition matrix element squared

$$|H_{ij}^D| = | < j|H^D|i > |^2, \tag{2.38}$$

where i and j stand for initial and final state, and $|H_{ij}^D|$ yields the expectation value of the dipole operator squared.

The oscillator strength is thus defined as

$$f = \frac{2N\omega_0}{\epsilon_0 \hbar}|H_{ij}^D|, \tag{2.39}$$

and expresses the probability of absorption or emission of electromagnetic radiation in transitions between energy levels of an atom or molecule.[14]

2.2 Experimental Method

The purpose of this section is to introduce the reader to the characterization method used in the present work.

2.2.1 Photoluminescence Spectroscopy

Photoluminescence is the spontaneous emission of light from a material under optical excitation. Photoluminescence spectroscopy is a widely used and efficient technique for the analysis of the optoelectronic porperties in semiconductors. By applying external light with energy $hv \geq E_g$, the reemitted photons can give detailed information on discrete electronic states, involving intrinsic and extrinsic optical processes, including internal transitions involving defects and their energy levels. One of its biggest advantages is that it is a non-destructive, contactless, technique, which provides electrical characterization of our samples.

Photoluminescence depends on the nature of the optical excitation. The excitation energy governs the penetration depth of the incident light. The density of photoexcited electrons contributes to the photoluminescence signal output, and can be controlled by adjusting the intensity of the incident beam. If the type or quality of the material in the sample varies spatially, the photoluminescence signal will change with excitation position. Furthermore, pulsed optical

excitation provides powerful means for studying the brief changes in the state of our physical system. In time resolved photoluminescence spectroscopy, short laser pulses produce virtually instantaneous excited populations after which the photoluminescence signal can be monitored to study recombination events.

Photoluminescence spectroscopy can be used for bandgap determination, separating and analysing radiative and non-radiative recombination processes. Furthermore is detecting and identifying defects and impurity levels possible. The photoluminescence energy associated with these levels can be used to identify specific defects. An assessment of material quality can be made by quantifying the radiative recombination. Photoluminescence spectroscopy is also widely used when it comes to the study of surfaces. PL often originates near the surface of a material, and photoluminescence analysis becomes an important tool in the characterization of surfaces.

There are also some limitations to photoluminescence spectroscopy. Among those is the fact that PL spectroscopy proves inefficient when it comes to the study of recombination mechanisms at deep states as the radiative transitions give a very broad spectra. This can be a result of e.g strong phonon coupling. Materials dominated by non-radiative recombination mechanisms are difficult to study as the entire method of photoluminescence spectroscopy relies on radiative events.[13, 17]

A typical set-up for photoluminescence measurements can be found in figure 2.11.

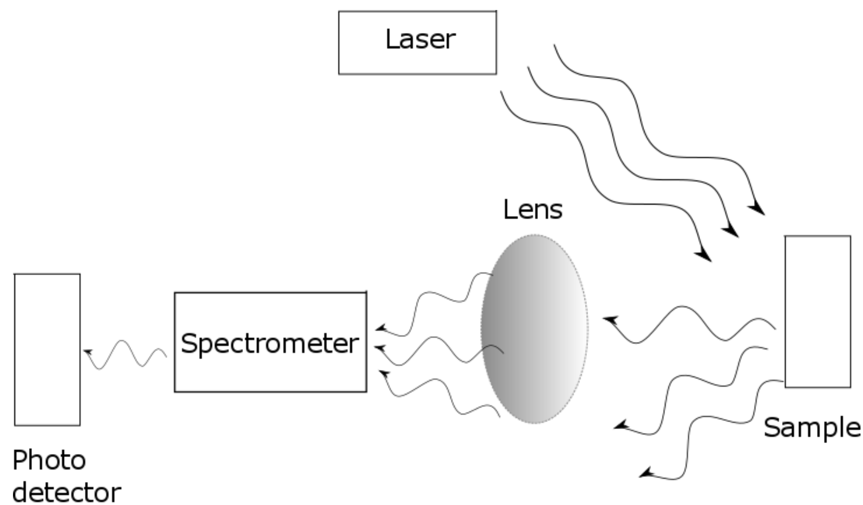

Figure 2.11: A typical experimental setup for photoluminescence measurements

2.3 Theoretical Method

Here an explanation of the primary method of the present study is presented. A closer look is provided on the Poisson equation, theoretical approach to strain and two essential concepts of $k \cdot p$ perturbation theory with respect quantum mechanical modelling, namely the single- and multi-band single envelope function approximations.

2.3.1 Poisson Equation

The Poisson equation deals with electrostatics within our model and reads as follows

$$\bigtriangledown \cdot [\epsilon_0 \epsilon_r(x) \bigtriangledown \phi(x)] = -\rho(x). \tag{2.40}$$

Here ϵ_0 is the permittivity of vacuum, ϵ_r the material dependent static dielectric constant, and ϕ the electrostatic potential. The dielectric function is anisotropic for wurtzite structures and isotropic for zincblende. The charge density distribution $\rho(x)$ reads

$$\rho(x) = e[-n(x) + p(x) + N_D^+(x) - N_A^-(x) + \rho_{fix}(x)], \tag{2.41}$$

where e is the elementary charge, n and p are the electron and hole densities. $N_D^+ +$ and N_A^- are the concentrations of ionized donors and acceptors.

ρ_{fix} represents fixed interface or volume charge densities, and may be taken into account if they arise from piezo- or pyroelectric charges. The densities can be calculated either classically, by the Thomas-Fermi approximation, or quantum mechanically. The Poisson equation is discretized on a non-uniform grid with a finite-difference method, which is the dominant approach to partial differential equations, and solved numerically by Newton's method. As previously mentioned, the unique solution of the Poisson equation requires specifying boundary conditions. Typically we use Neumann boundary conditions for the Poisson equation, which suggests a vanishing electric field at the boundaries.

$$\partial \phi / \partial x = 0 \tag{2.42}$$

In the case of non-equilibrium simulations, Dirichlet boundary conditions are used. In this case the built-in potential first has to be determined using Neumann boundary conditions. Then the electrostatic potential is fixed, according to Dirichlet, at the boundaries with respect to the chemical potentials taking into account the calculated built-in potential. If there are any contacts present in the simulation, the chemical potentials of these are fixed and correspond to the applied bias.[8, 18]

An overview of a possible program flow in $next$**nano**^{3} is provided in Fig. 2.12.

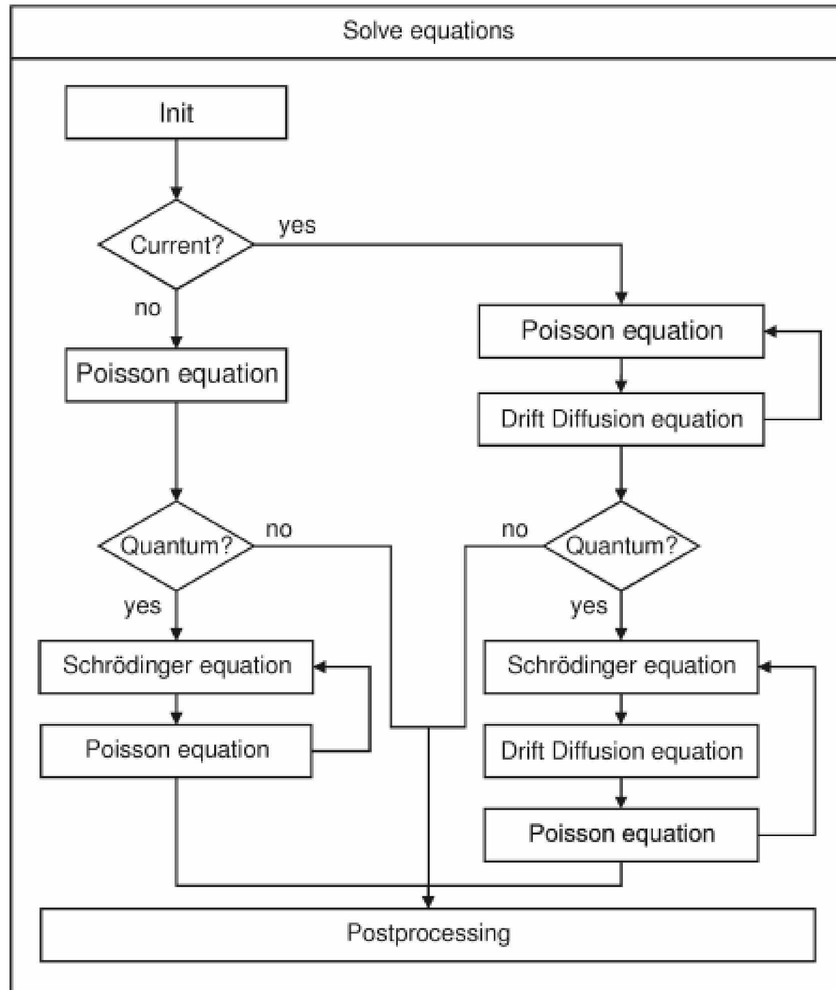

Figure 2.12: Flowchart of the self-consistent solution of the Schrödinger, Poisson, and current equations. Original figure can be found in[8].

2.3.2 Strain

Strain has two major effects on semiconductors which we have to account for in our simulations.

- Strain is responsible for piezoelectric polarization charges, contributing to the charge density in the Poisson equation and changing the electrostatic potential.
- Strain directly influences the electronic structure by inducing shifts in the band edges via the deformation potentials.

Furthermore, strain can be used to alter and optimize the electronic and optical properties of our quantum wells by varying both the energy levels and the spatial extent of the wavefunctions. As we are working with heterostructures comprised of semiconductor materials with different lattice constants, it is important to note that they are subject to elastic deformations. The effects of these deformations on the lattice changes drastically with the growth direction. It goes without saying that an exact knowledge of strain effects is of importance to interpretation of data

as well as being an important tool for device engineers in altering the electronic structure of semiconductor devices.

In ii-vi semiconductors, strain is followed by a displacement of the centres of positive and negative charges within a unit cell, leading to the formation of electric dipoles. These microscopic dipoles are not compensated in the case of inhomogeneous strain fields, at interfaces or surfaces, and as such yield macroscopic polarization charges called piezoelectric charges. In the wurtzite crystal structure we also find a permanent polarization, independent of strain, along the c-axis. This leads to macroscopic polarization charges at surfaces and interfaces which are termed pyroelectric charges.

A nth rank tensor in m-dimensional space is a mathematical object that has n indices and m^n components, and obeys certain transformation rules. Each index of a tensor ranges over the number of dimensions of space. Elasticity theory gives us a number of tensors, these tensors are only characterized by a small number of elasticity constants due to symmetry in the crystals. The diagonal elements of the strain tensor measure the extensions per unit length along the coordinate axes, positive values yield tensile strain, while negative yield compressive strain). In principle this means that the lengths of the considered volume element change while the angles remain constant. The off-diagonal elements measure the shear deformations where the volume remains constant and the angles change.

The piezoelectric polarization is proportional to the strain tensor

$$P_{piezo} = e_{ijk}\epsilon_{jk} \tag{2.43}$$

Where proportionality constants form a third rank tensor e_{ijk}. In Voigt notation we get one non-zero component for zincblende and three for wurtzite. The three non-zero components in the case of wurtzite crystal structure are e_{15}, e_{31}, and e_{31}. For the relation between the piezoelectric polarization vector and the strain tensor the following equation holds:

$$P_{piezo,wz} = \begin{pmatrix} 2e_{15}(x)\epsilon_{13}(x) \\ 2e_{15}(x)\epsilon_{12}(x) \\ e_{31}(x)\epsilon_{11}(x) + e_{31}(x)\epsilon_{22}(x) + e_{33}(x)\epsilon_{33}(x) \end{pmatrix}$$

To obtain the full polarization vector for wurtzite crystal structure the contribution

$$P_{piezo,wz} = \begin{pmatrix} 0 \\ 0 \\ \rho(x) \end{pmatrix}$$

of the pyroelectric polarization has to be added. Here $\rho(x)$ is the material dependent pyroelectric constant.[8]

$$\mathbf{P_{pol,wz}}(x) = \mathbf{P_{piezo,wz}}(x) + \mathbf{P_{pyro,wz}}(x) \tag{2.44}$$

In regions where $P_{pol}(x)$ is constant, there are no polarization charges present. This is not necessarily the case at interfaces, where the piezo- and pyroelectric constants undergo an abrupt change from one material to another. In this case polarization charges are likely to occur. The same will be the case for position independent piezoelectric constants in inhomogeneous strain fields.

In the $next$**nano**^{3} software, strain is calculated prior to all other equations, and is therefore considered independent of these. The separation of strain from the main part of the program is not fully justified in the case where strong pyroelectric fields exist, e.g in the wurtzite structure.[18]

2.3.3 Single-band Envelope Function Approximation (Effective Mass Approximation)

In theoretical modelling of semiconductor devices, it is often useful to use $k \cdot p$ perturbation theory as an approximation scheme for calculation of the bandstructure and optical properties of our crystalline solids. Perturbation theory comprises mathematical methods for finding an approximated solution to a problem by starting from the exact solution of a simpler problem. This is very useful if the problem can't be solved exactly, but can instead be formulated by adding small terms to the mathematical description of the exact solvable problem. An approximation for the solution of P with a small parameter ϵ can be written as the series

$$P = P_0 + \epsilon^1 P_1 + \epsilon^2 P_2 + ... \tag{2.45}$$

Where the higher terms of ϵ becomes smaller and smaller. An approximate solution to this is found by truncating the series.

The $k \cdot p$ approximation exploits the fact that many properties of semiconductors depend solely on the shape and position of the extrema of the conduction and valence bands at $\mathbf{k} = \mathbf{0}$, and as such a precise knowledge of the entire bandstructure is not needed. To achieve a good approximation we therefore expand the dispersion relation $E_n(\mathbf{k})$ around these extrema at $\mathbf{k_0}$ up to the second order in $|\mathbf{k} - \mathbf{k_0}|$ and rewrite the Hamiltonian.

$$H(\mathbf{k}) = H(\mathbf{k_0}) + \frac{\hbar}{m}(\mathbf{k} - \mathbf{k_0}) \cdot \mathbf{p} + \frac{\hbar^2}{2m}(\mathbf{k} - \mathbf{k_0})^2 \tag{2.46}$$

The single-band Schödinger equation is a special case of the 8×8 $k \cdot p$ Schrödinger equation, which will be further discussed in the next section. If the coupling between valence and conduction band is ignored, i.e electrons and holes are decoupled, one obtains a twofold degenerate Schrödinger equation for the electrons in a heterostructure. This is the same as the Effective Mass Approximation. We recall the Schrödinger equation

$$\mathbf{H}\Psi_n(x) = E_n \Psi_n(x) \tag{2.47}$$

The Hamiltonian now becomes

$$(-\frac{\hbar^2}{2}\nabla \cdot M(x)\nabla + V(x))\Psi_n(x) = E_n\Psi_n(x) \tag{2.48}$$

Since we are dealing with electrons, $V(x)$ becomes the resulting conduction band edge profile including band shifts due to strain, electrostatic potential and the band offsets. As we remember, each index of a tensor ranges over the number of dimensions of space. $\mathbf{M}$ is the tensor describing the effective mass to allow for different values along the directions

$$M = \begin{pmatrix} 1/m_{xx} & 1/m_{xy} & 1/m_{xz} \\ 1/m_{yx} & 1/m_{yy} & 1/m_{yz} \\ 1/m_{zx} & 1/m_{zy} & 1/m_{zz} \end{pmatrix}.$$

M generally assumes the form of an ellipsoid, but it is spherical for electrons at the Γ point with its eigenvalues on the diagonal. This approximation gives a good description of the electron valleys at the center of the Brillouin zone. The L and X, in the case of a non-corresponding simulation and crystal system, points do however need off-diagonal components to describe the electron masses. For a good description of the entire system it is therefore necessary to solve several Schrödinger equations with the same V(x), but with different effective mass tensors. In the case of band edges being split due to strain, each Schrödinger equation will also have a different V(x).

In the case of wurtzite, which we know to be hexagonal and not cubic, a spherical effective mass tensor is no longer appropriate at the Γ point. It is necessary to differentiate between the mass parallel to the c-axis, $m_{\|}$, and the two masses perpendicular to it, $m_{\perp}$. The inverses of these masses comprise the diagonal components of the effective mass tensor.

It is possible to use the same Schrödinger equation for all the valence bands, i.e heavy, light and split-off holes. The different band edges are in that case taken as V(x). The single-band model with a spherical mass is in general not very accurate for holes, and even less so if strain is present. This is because the energy dispersion $E(\mathbf{k}$ is no longer isotropic. The single-band model does however describe the ground state of heavy holes in heterostructures quite well, and can give a qualitative picture of the physics in our semiconductor device, e.g for electron-hole interband transition energy as a function of quantum well width, electric field, alloy composition etc.

As it takes considerable less time to run an effective mass approximation than a 8×8 $k \cdot p$ simulation, one may use the single-band to optimize the modelling file before running more computer heavy calculations.

Seeing as we in many cases are interested in the single-band Schrödinger equation for heterostructures in real space, as it may give us a better understanding of our semiconductor device, a real symmetric eigenvalue problem arises that is solved iteratively.[8, 14, 16, 18]

2.3.4 Multi-band $k \cdot p$ Envelope Function Approximation

A more accurate description of the bandstructure may be obtained by using the multi $k \cdot p$ methods. These differ mainly in the number of bands taken into consideration. If you consider many enough bands, the predictions yielded are close to perfect, but the computational force and time required is accordingly greater. The $next\mathbf{nano}^3$ software makes use of the 6×6 and 8×8 $k \cdot p$ model, in the case of 8×8 the lowest conduction band and the three highest valence bands are included, while all other remote bands are treated as perturbations. Spin-orbit interaction and strain are taken into account.

The key feature of the $k \cdot p$ method is the envelope function ansatz based on Bloch's theorem. As we recall from previous chapters the electron wave function in a crystal can be separated into an oscillating Bloch part which is periodic over atomic distance, and a smooth envelope function which varies at a greater scale.

We recall

$$H(\mathbf{k}) = H(\mathbf{k_0}) + \frac{\hbar}{m}(\mathbf{k} - \mathbf{k_0}) \cdot \mathbf{p} + \frac{\hbar^2}{2m}(\mathbf{k} - \mathbf{k_0})^2. \tag{2.49}$$

The Bloch factors $u_{n,\mathbf{k_0}}$ for $\mathbf{k} = \mathbf{k_0}$ obey

$$H(\mathbf{k_0})u_{n,\mathbf{k_0}} = [\frac{(\mathbf{p} + \hbar\mathbf{k_0})^2}{2m} + V_{ion}(x) + V(n)]u_{n,\mathbf{k_0}} = E_n(\mathbf{k_0})u_{n,\mathbf{k_0}}, \tag{2.50}$$

and form a complete set of orthonormal functions, meaning that we can expand the Bloch factors for an arbitrary value of $\mathbf{k}$

$$u_{n,\mathbf{k}}(x) = \sum_v c_{n,v}(\mathbf{k})u_{n,\mathbf{k_0}}(x). \tag{2.51}$$

Rewriting we get the expression

$$E_n(\mathbf{k})c_{n,v}(\mathbf{k}) = \sum_\mu H_{v\mu}(\mathbf{k})c_{n,\mu}(\mathbf{k}). \tag{2.52}$$

And so the Hamiltonian can be represented by the infinite dimensional matrix that couples all energy bands by means of the momentum matrix elements $\mathbf{p}_{v\mu}$ between the respective Bloch factors for $\mathbf{k} = \mathbf{k_0}$

$$H_{v\mu}(\mathbf{k}) = [E_v(\mathbf{k_0}) + \frac{\hbar^2}{2m}(\mathbf{k} - \mathbf{k_0})^2]\delta_{v\mu} + \frac{\hbar}{m}(\mathbf{k} - \mathbf{k_0}) \cdot \mathbf{p}_{v\mu}. \tag{2.53}$$

The rapidly oscillating Bloch functions may be eliminated from the electron Hamiltonian according to Löwdin perturbation theory, limiting the infinite dimensional Hamiltonian matrix to one with finite dimensions.

As previously mentioned $next\mathbf{nano}^3$ utilizes 6×6 and $8\times8 k{\cdot}p$. In the 6×6 $k{\cdot}p$ Hamiltonian, all conduction bands are considered as perturbation. In the 8×8 case the lowest conduction band

is no longer treated as a perturbation, but included in the $k \cdot p$ Hamiltonian. The related material parameters for 8×8 $k \cdot p$ are thus different from those in the 6×6 $k \cdot p$ case. [16, 14, 18]

2.3.5 Spurious Solutions

When numerically implementing the $k \cdot p$ Hamiltonian, one will sooner or later encounter spurious solutions. These are unphysical wavefunctions that look strange. They might materialize by displaying very strong oscillations, or they may show spikes at material interfaces. Occasionally, their energies can be found lying within the forbidden band gap. The spurious solutions might arise from incorrect discretization, or from the used $k \cdot p$ parameters. [18]

2.3.6 Boundary Conditions for the Schrödinger Equation

When choosing boundary conditions for the Schrödinger equation we are left with Neumann and Dirichlet Boundaries. These boundary conditions appear in several places in our theoretical method: The unique solution of the Poisson equation requires specifying boundary conditions. Boundary conditions have to be specified at the boundaries of the nanostructure, and furthermore, they are also used at the interfaces of contacts. We will in this case choose to talk about them in the framework of the Shcrödinger equation.

Neumann and Dirichlet Boundaries

The consequence of choosing either Dirichlet or Neumann boundary conditions, for the Schrödinger equation, depends on whether we have a shallow or a sloped potential.

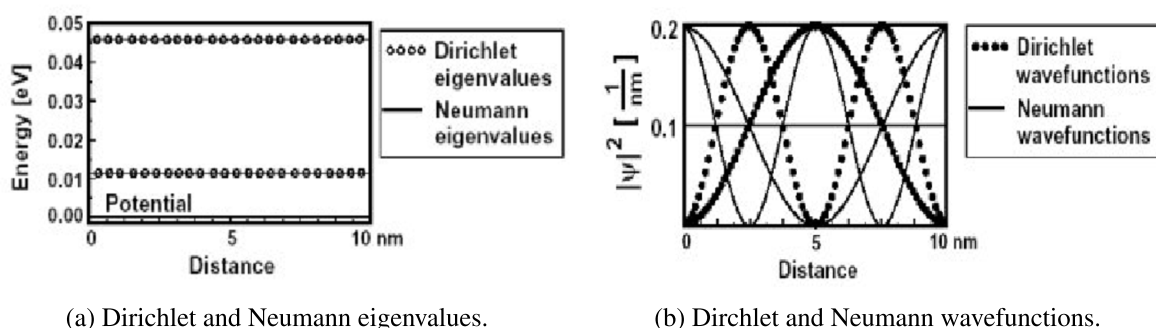

(a) Dirichlet and Neumann eigenvalues.

(b) Dirchlet and Neumann wavefunctions.

Figure 2.13: Dirichlet and Neumann wavefunctions and eigenvalues for a shallow potential. Figures originially from [19]

For a shallow potential, Dirichlet boundaries yield eigenfuctions with a cosine shape as it is the case of a potential well with infinitely high barriers. With Neumann boundaries one obtains the same eigenvalues, but as shown in figure 2.9, the eigenfunctions are shifted by a phase of $\frac{\pi}{2}$. The eigenvalue zero also occurs with a constant wavefunction.[19]

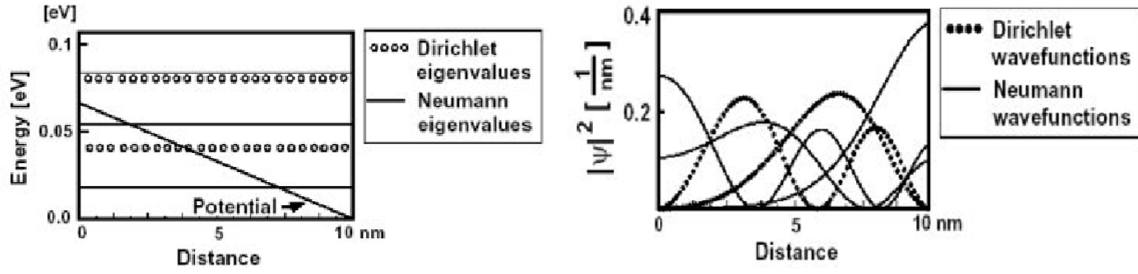

(a) Dirichlet and Neumann eigenvalues.

(b) Dirchlet and Neumann wavefunctions.

Figure 2.14: Dirichlet and Neumann wavefunctions and eigenvalues for a sloped potential. Figures originially from [19]

As we can see in the case of the sloped potential, the Dirichlet wavefunctions are forced to zero at the boundaries of the quantum region, while the Neumann wavefunctions do not have to meet this requirement and are found to be non-zero at the boundaries.

The mixed boundary condition

If one only solves the Schrödinger equation for an inner region in the sample, as is often the case for a SQW or MQW device, you can either choose Dirichlet or Neumann boundaries, as the states eventually will be normalized to 1, i.e a fully occupied state is equivalent to exactly one electron. At the interface between the inner region and the rest of the sample,the idealistic assumption that charge neutrality exists, and that the DOS is the same as in bulk material, is made. With pure Dirichlet boundary conditions, however, the density would decrease to zero at the interface whereas with Neumann boundary conditions the density would increase. Thus, it is reasonable to assume something like a mixed state. This means that we solve the Schrödinger equation once with Dirichlet and once with Neumann boundary conditions to normalize the states to 1/2. This is made plausible by looking at Fig 2.13. For the same eigenfunction one obtains one sine and one cosine function, the sum over both is constant. As both eigenfunctions are normalized to 1/2, the occupation of these mixed states corresponds to one electron.[8]

Chapter 3

Results and discussion

In this chapter the experimental and theoretical results, yielded from PL spectroscopy and quantum mechanical modelling respectively, are presented and discussed.

3.1 Photoluminescence Spectroscopy

Polar (0002) and non-polar (11-20) $Cd_xZn_{1-x}O/Mg_{0.08}$ ZnO MQWs (with x=0, 0.25, 1.0) were grown on C-plane (0002) and R-plane (01-12) oriented sapphire substrates by metal organic vapor phase epitaxy (MOVPE). The 4-period MQWs with different thicknesses $Cd_xZn_{1-x}O$, (x=0, 0.25, 1.0), QW layers were grown at 370°C with the chamber working pressure of 600 Torr. Diethyl zinc (DEZn) and dimethyl cadmium (DMCd) were used as group-II sources, and tertiary butanol (t-BuOH) was used as group-VI source. The DEZn and t-BuOH flows were fixed at 100 and 150 sccm, respectively for all samples, while DMCd flow was fixed at 25 and 75 sccm for $Cd_{0.25}Zn_{0.75}O$ and CdO QW, respectively. The thickness of the well and barrier layers was controlled by tuning the growth time according to the growth rate. More details on the MOVPE growth conditions are given in[20].

Time-resolved photoluminescence (TRPL) measurements were carried out on polar/nonpolar MQW structures (series 598) comprising X4 bilayers of 3nm-thick ZnCdO QW (Cd 25%) and 10nm MgZnO barrier (Mg 8%) on C- or R-Al2O3 substrates, respectively. Time-integrated (steady state) PL experiments were performed with abovementioned series along with MQW structures representing pure ZnO quantum wells, as well as MgZnO quantum wells. More specifically, (series 599 and 601) polar/non-polar 3nm-thick ZnO and $Mg_{0.03}Zn_{0.97}$ QW /10nm-thick MgZnO barrier (Mg 8%) X4 bilayers on C- or R- Al_2O_3 substrates.

Time-resolved photoluminescence (TRPL) properties of the Zn(Mg,Cd)O MQW structures were investigated in the 10K-300K temperature range by employing 372nm wavelength laser (PicoQuant, 50ps-pulsed, average power 2mW @40MHz) as an excitation source. In addition, cw 325nm HeCd laser (7mW) was used for acquisition of time-integrated spectra and for micro-imaging of PL patterns. The luminescence from the sample was collected by a long working distance microscope and then directed both to imaging spectrograph (HORIBA Jobin Yvon,

iHR320) with two exit ports coupled to EMCCD camera (Andor DL-658M) and photon counting PMT (Becker&Hickl, PMC100) and also to fiberoptic spectrometers (Ocean Optics, HR4000 and USB4000 with 0.2/2nm spectral resolutions, respectively). Low temperature measurements were performed using closed-cycle He-refrigerator (Janis, Inc., CCS450).

Schematic sketches of optical configuration and block diagram of the experimental setup are presented in figure 3.1 and 3.2, respectively.

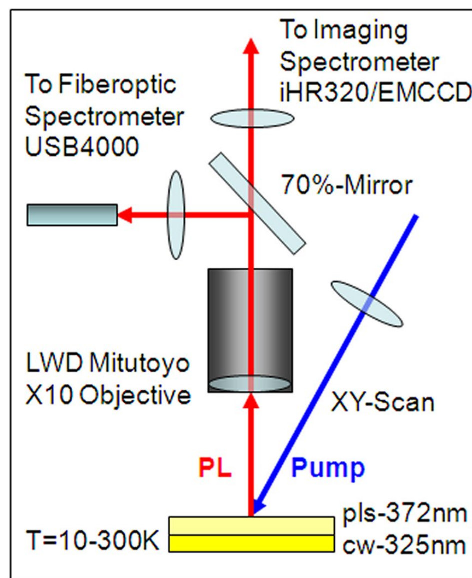

Figure 3.1: Optical configuration of the PL and TRPL experiments

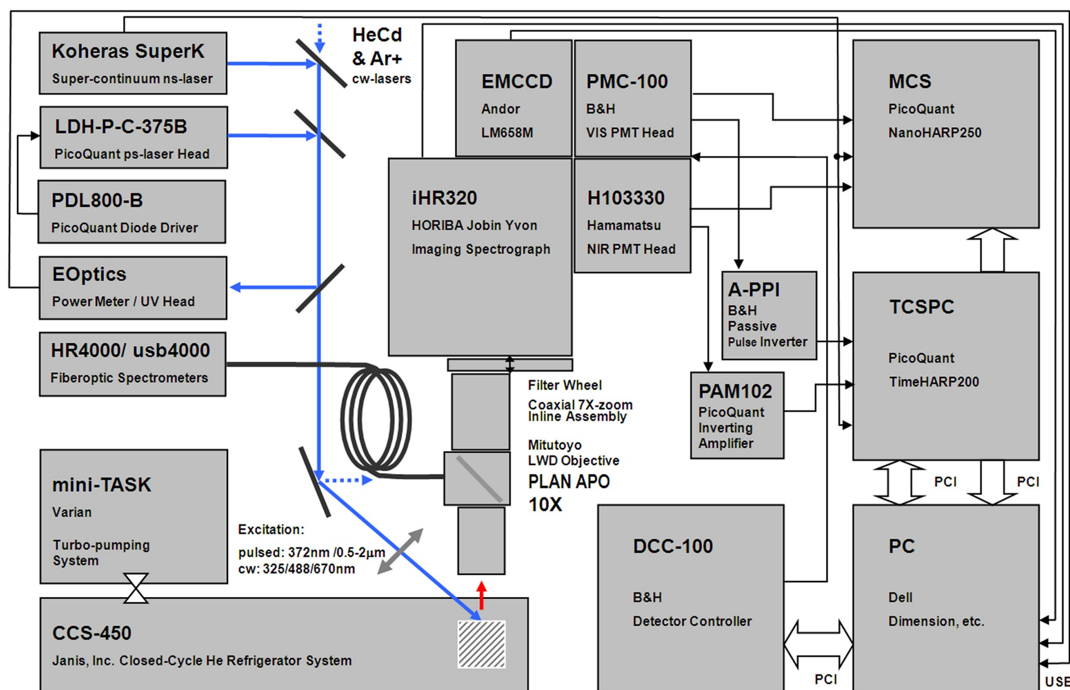

Figure 3.2: Schematic diagram of the PL/TRPL setup

3.1.1 Time-Integrated (Steady State) Photoluminescence Spectroscopy

The steady state PL measurements of our structures were carried out as explained in section 2.1. The resulting PL spectra of polar ZnCdO/MgZnO MQW at various temperatures is representative for our measurements, and can be found in Fig. 3.3.

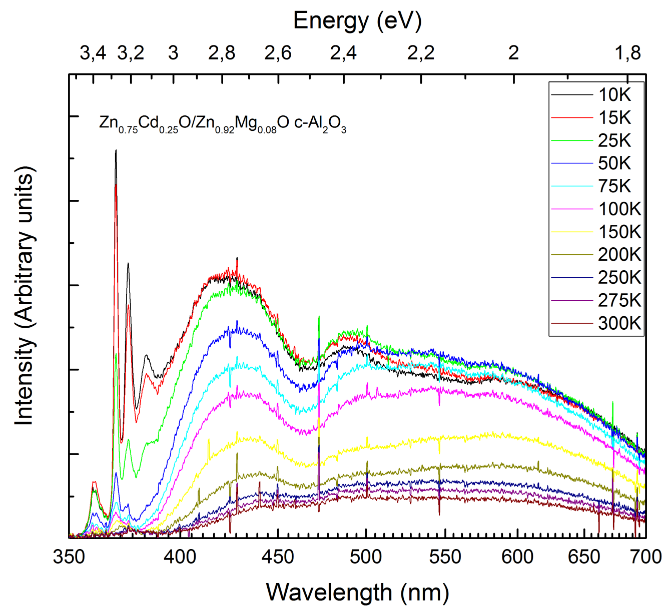

Figure 3.3: PL spectrum in linear scale of the polar ZnCdO/MgZnO MQW at various temperatures.

A decrease in efficiency of the luminescence is shown with increasing temperature, this thermal quenching of the photoluminescence intensity indicates an opening of competing non-radiative relaxation pathways. The barriers are found to be emitting non-negligible photoluminescence, this can be an indication of varying quality of interfaces and thus efficient relaxation processes. A closer look at the high energy peak positions is given by high resolution PL measurements at 10K in Fig. 3.4,

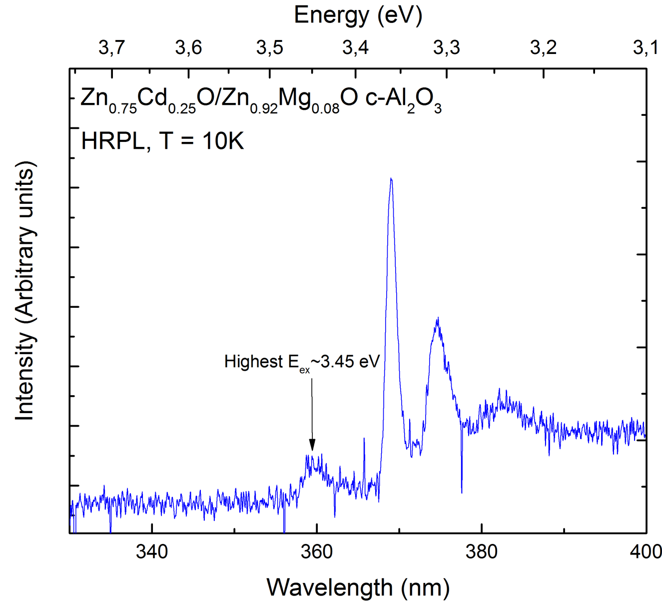

Figure 3.4: High resolution PL spectrum of the polar ZnCdO/MgZnO MQW at 10K.

where we find the highest excitonic line at 10K corresponding to ~3.45 eV. As we remember ZnO structures have exciton binding energies of the order 60meV, which certainly holds for low temperatures, meaning that what we are seeing is actually the exciton line found slightly below the conduction band edge.

The temperature dependent PL intensity of a quantum well is described by a modified two channel Arrhenius fit function

$$I(T) = \frac{I(0)}{1 + C_1 \cdot exp(-E_1/kT) + C_2 \cdot exp(-E_2/kT)}. \quad (3.1)$$

Where I(T) is the integrated PL intensity at temperature T, k is the Boltzmann constant, E denotes activation energy, while C is a tunneling factor and $I(0)$ is the integrated intensity at the temperature limit.

The activation energies found using this fit for integrated PL intensity at peak positions as a function of temperature in our samples are shown in Fig. 3.5.

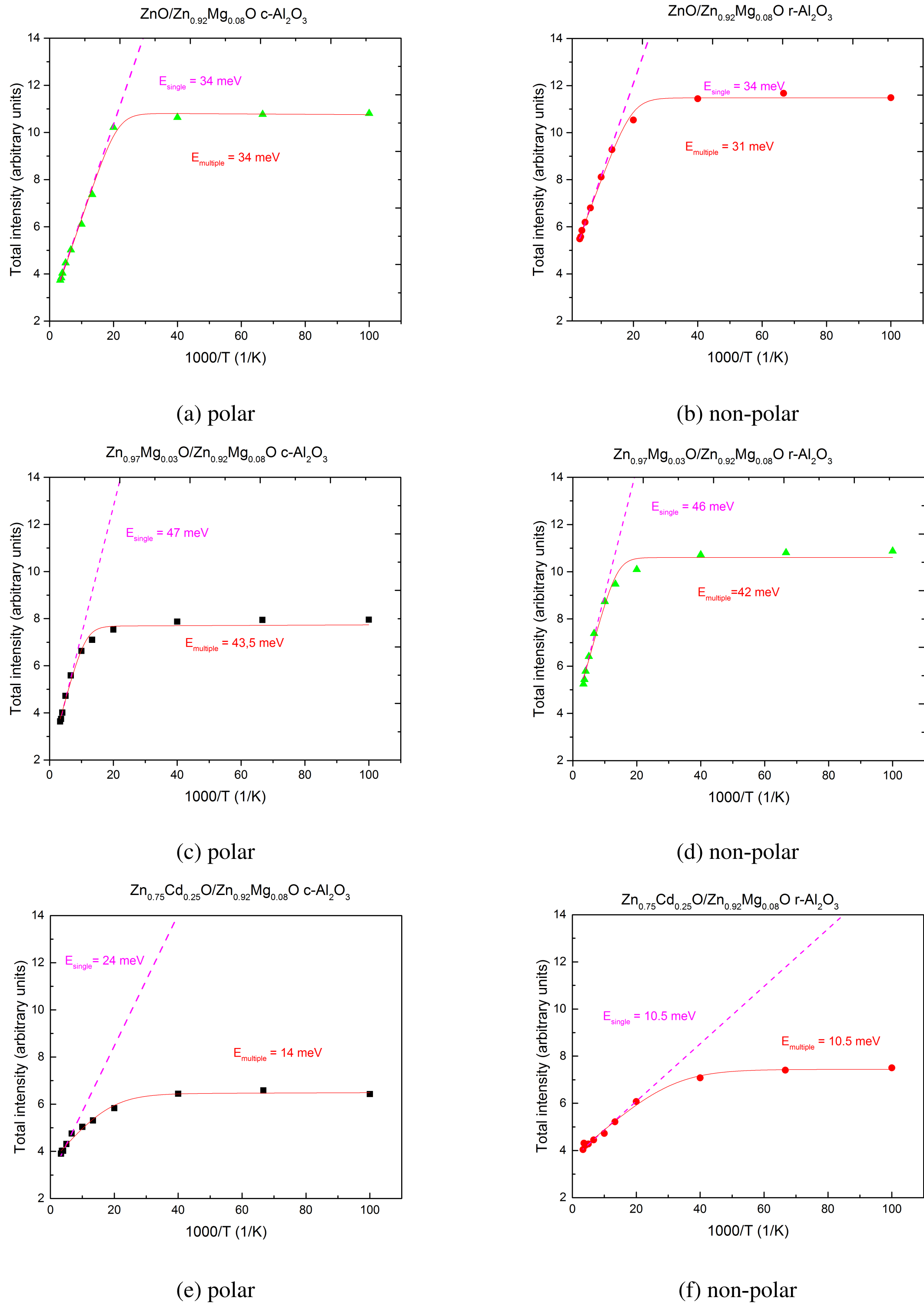

(a) polar (b) non-polar

(c) polar (d) non-polar

(e) polar (f) non-polar

Figure 3.5: Integrated PL intensity plotted versus temperature with Arrhenius single and multiple fit functions.

The relatively low activation energies found in the regime 10-14 meV, are likely to correspond to a localization energy or ionization energy of donor bound excitons. Values around 30 meV can likewise be contributed to a localization or ionization energy of acceptor bound excitons. Activation energies of 45-55 meV are in turn likely to correspond to exciton binding energies

in our different samples[21, 22]. Free excitons in bulk material ZnO is well known to have binding energies of about ∼60 meV. In quantum well heterostructures it is also possible to find activation energies of the order $\sim 10^2$ meV corresponding to the energy required for a carrier escaping from the well into the surrounding barriers.[23]

3.1.2 Time Resolved Photoluminescence Spectroscopy

The samples under investigation using time resolved photoluminescence spectroscopy were grown as specified in section 3.1

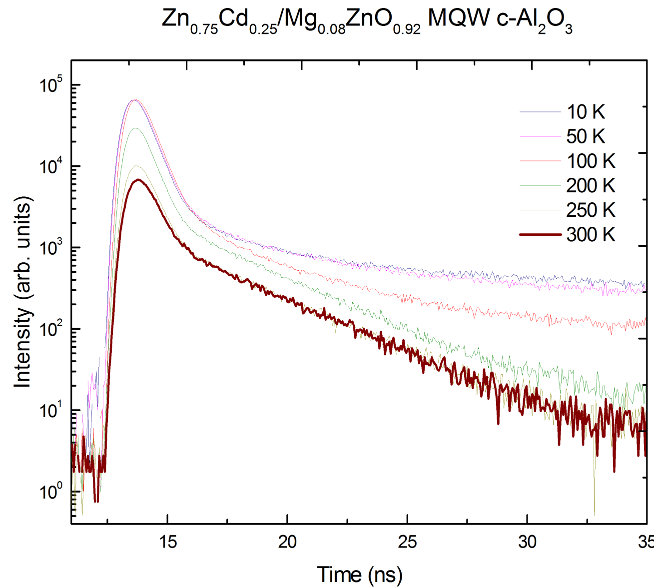

Figure 3.6: Photoluminescence intensity decay after pulsed excitation at various sample temperatures for a $c-$plane ZnCdO/ZnMgO MQW structure.

The decay corresponding to the central wavelengths of 390 and 420nm were measured as a function of temperature as shown in figure 3.6. Typically it is possible to observe a reduction of the height and a change of the time dependence of the transients with increasing temperature. The transient parameters I_0, corresponding to the initial intensity, and τ, corresponding to the intensity decay time, have both been taken from single-exponential fits in appropriate time intervals, as is illustrated in figure 3.7. Correcting for the system response function allows us to gain relevant information on radiative and non-radiative lifetimes in our samples.

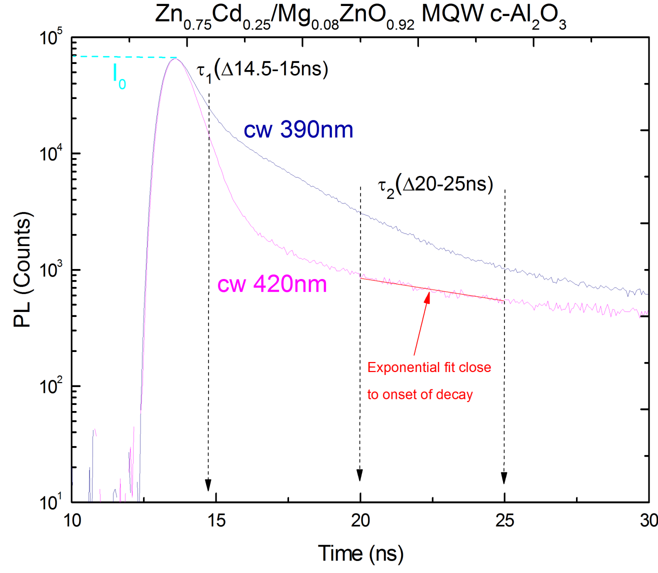

Figure 3.7: Photoluminescence intensity decay after pulsed excitation at 10K for a c-plane ZnCdO/ZnMgO MQW structure. The dashed lines illustrates the parameter I_0. while the red line represents the single-exponential fit within one of the time intervals, illustrated by the dashed arrows, taken into account, in this case τ_2.

The measured time decay τ_L at a temperature T is related to the radiative and non-radiative recombination times τ_R and τ_{NR}, respectively, by

$$\frac{1}{\tau_L(T)} = \frac{1}{\tau_R(T)} + \frac{1}{\tau_{NR}(T)}. \tag{3.2}$$

It is further supposed that the carriers in the levels which undergo recombination are at thermal equilibrium, i.e the thermalization processes are much faster than the recombination processes. This implies that there is a strong coupling between these states, so that a single time constant will describe the radiative processes inside the whole PL band. The same will then also hold true for the non-radiative processes.

At the same time, the temperature dependence of the luminescence intensity, denoted $I_L(T)$, integrated over the whole PL band can be expressed as

$$I_L(T) = I_0 \frac{\tau_L(T)}{\tau_R(T)} = I_0 \eta(T), \tag{3.3}$$

where $\eta(T)$ is the radiative efficiency at temperature T, and I_0 serves as a normalization factor that depends on the number of photoexcited carriers.

From equations 3.2 and 3.3, it follows that

$$\tau_R(T) = I_0 \frac{\tau_L(T)}{I_L(T)} = \frac{\tau_L(T)}{\eta(T)}, \tag{3.4}$$

$$\tau_{NR}(T) = \tau_L(T)\frac{I_0}{I_0 - I_L(T)} = \tau_L(T)\frac{1}{1-\eta(T)}. \quad (3.5)$$

It is therefore possible to extract both the radiative and non-radiative recombination times, as a function of T, from the combined measurements of τ_L and $I_L(T)$. [24]

In figure 3.8 one can see the lifetimes τ_2 of the two central wavelengths as a function of temperature. τ_2 corresponding to cw 390nm is shown to oscillate between values of 2ns, and does not provide us with much information. The central wavelength of 420nm was therefore chosen to determine the radiative and non-radiative carrier lifetimes. of τ_1 and τ_2.

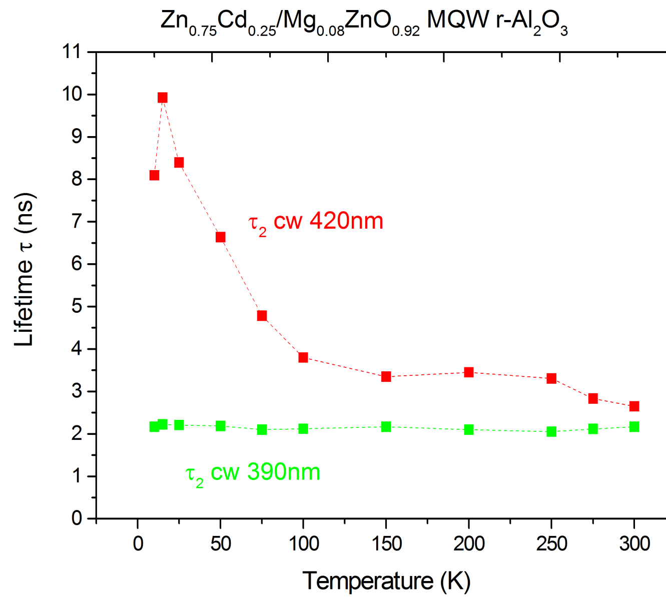

Figure 3.8: Lifetimes τ_2 of the two central wavelengths plotted against each other as a function of temperature.

The extraction of radiative and non-radiative lifetimes were done as described in Eqs. 3.2-5 for the polar and non-polar case, and is shown below. For the measured lifetimes, τ_1, τ_2 in the different samples it is shown that at low temperatures the non-radiative lifetimes are long, indicating slow recombination processes. Subsequently the radiative lifetimes are low, yielding rapid recombinations, meaning that these processes dominate at low temperatures.

A transition between radiative and non-radiative lifetimes is found at 100K for τ_1 and τ_2 in the polar samples, while this transition occurs at 50K in the non-polar case, indicating a more rapid opening of competing, non-radiative, pathways in the non-polar ZnCdO/MgZnO than is found for the polar case.

At high temperatures the non-radiative recombination processes are dominating for all the samples. This is in accordance with the thermal quenching noticed in the steady state PL measurements of the polar ZnCdo/MgZnO MQW structure in section 3.1.1

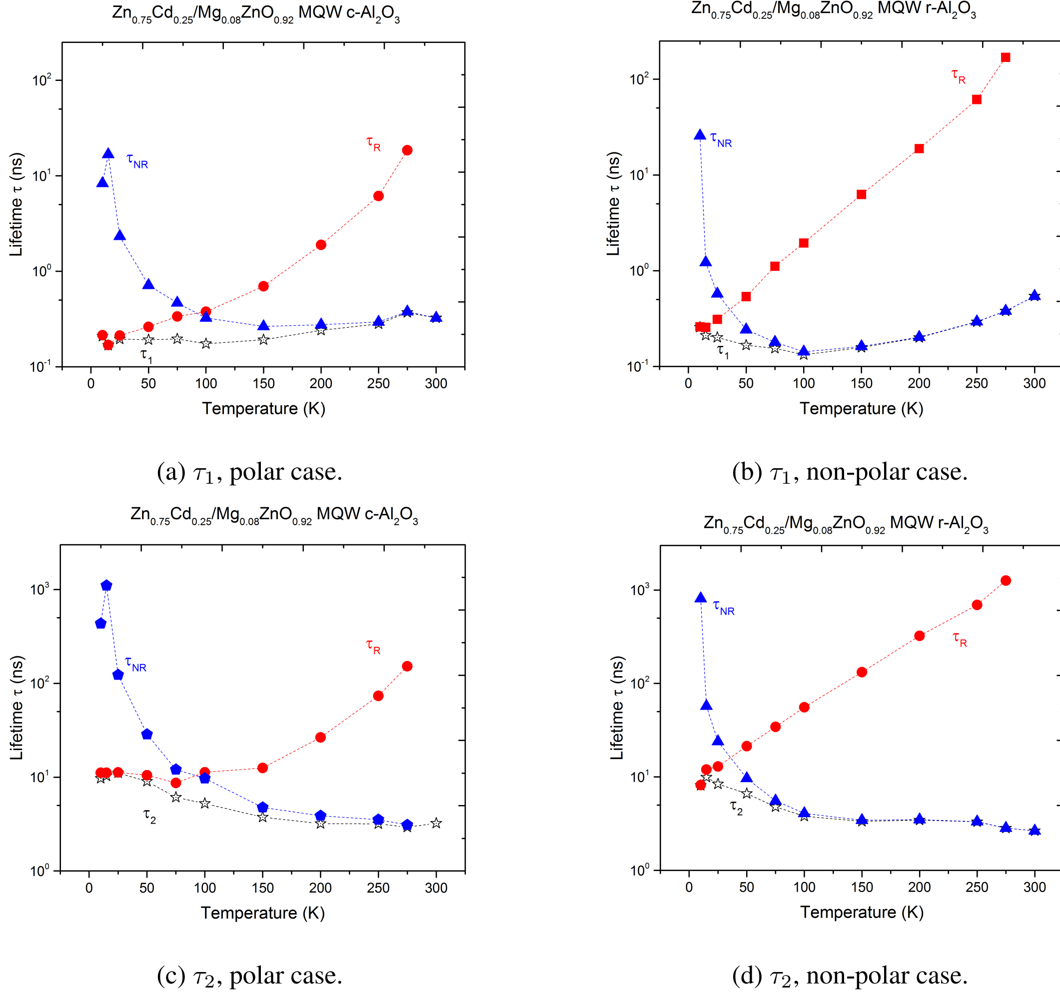

(a) τ_1, polar case.

(b) τ_1, non-polar case.

(c) τ_2, polar case.

(d) τ_2, non-polar case.

Figure 3.9: Separation of radiative and non-radiatve lifetimes in our polar and non-polar ZnCdO/MgZnO heterostructures

A low temperature measurement of lifetimes varying with well width was conducted on a very similar system with $Zn_{0.75}Cd_{0.25}O$ quantum wells with ZnO barriers. It is clearly shown in Fig. 3.10 (a) that the carrier lifetimes increased as a function of increasing well width in the polar case, while this dependency is not shared by the non-polar sample. A measure of the lifetime τ_2 versus temperature is shown in Fig. 3.10 (b).

With a well width of $L_w = 3nm$ we see a discrepancy in lifetimes between the polar and the non-polar case. This discrepancy is also found in the case of $Zn_{0.92}Mg_{0.08}O$ barriers, indicating that the two systems operate in a similar manner with respect to the polar and non-polar cases. The quantum confined Stark effect(QCSE) slows down radiative recombination dynamics [22], which is what happens when we increase the well width in our polar heterostructure and the QCSE begins to dominate. The increase in lifetimes is in good agreement with expected trends associated with the increased electron-hole separation and corresponding reduction of the oscillator strength[25]. The oscillator strength is also shown to be a lifetime related term. The lifetime τ_i can be expressed as

$$\frac{1}{\tau_i} = \sum_k A_{ik}, \tag{3.6}$$

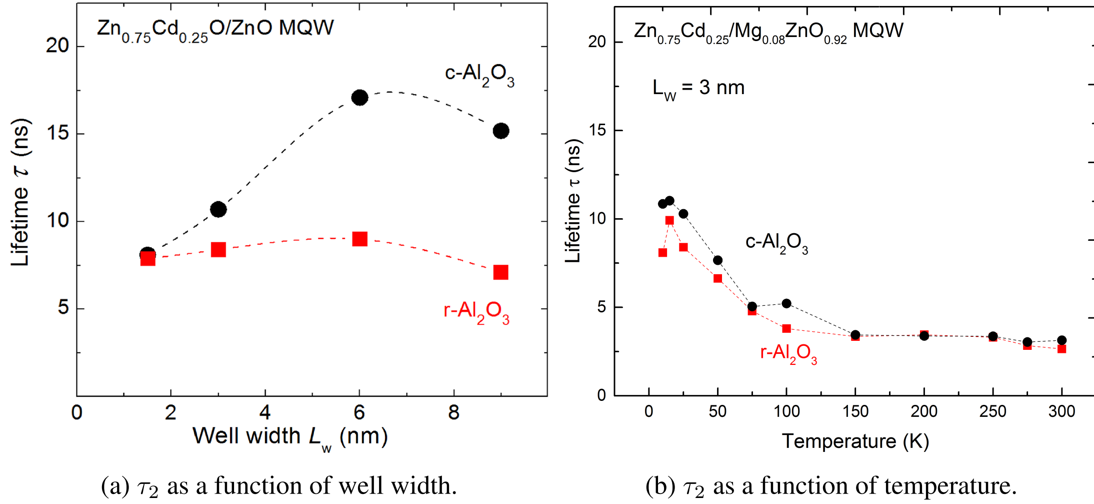

(a) τ_2 as a function of well width.

(b) τ_2 as a function of temperature.

Figure 3.10: Measurement of τ_2 as a function of well width at low temperatures in ZnCdO/ZnO heterostructures, and a similar ZnCdO/ZnMgO 3nm MQW heterostructure as a function of temperature.

where A_{ik} is the spontaneous transition rate given as the probability per unit time(s^{-1}) for an atom in any state of energy level i to make a transition to any state corresponding to energy level k. The oscillator strength is proportional to the spontaneous transition rate, $f \propto A_{ik}$ [26]. Oscillator strengths and the quantum confined Stark effect will be further discussed in the context of quantum mechanical modelling.

As a concluding matter the time resolved photoluminescence spectroscopy, lifetimes τ_1 and τ_2 were plotted as a function of inverese temperature, and then fitted with an Arrhenius multiple fit function. The activation energies extracted are in good accordance with the values yielded by the time-integrated photoluminescence spectroscopy, and can be found in figure 3.11

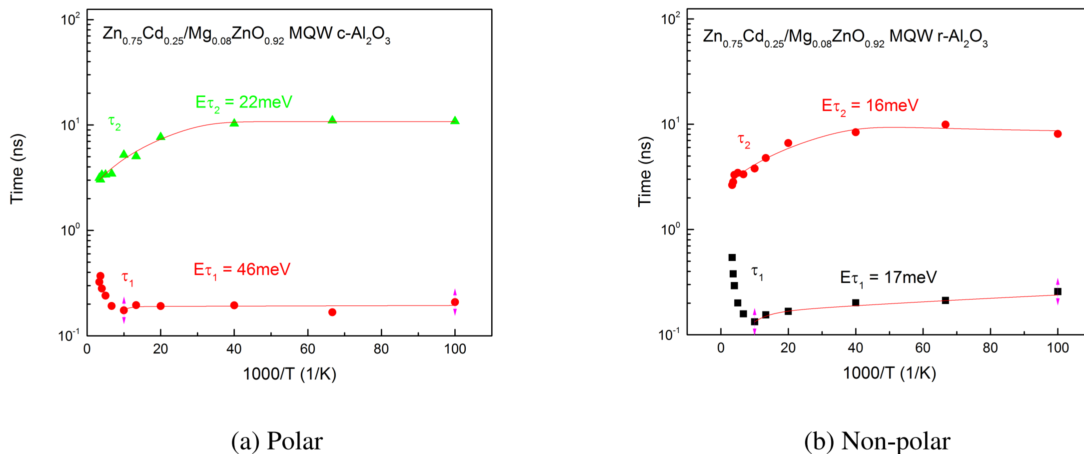

(a) Polar

(b) Non-polar

Figure 3.11: Arrhenius multiple channel fit of τ_2 plotted as a function of inverse temperature.

3.2 Quantum Mechanical Modelling

The quantum mechanical modelling was performed using the single-band(effective mass) envelope and the multi-band $k \times p$ envelope function approximation. The effective mass approximation is a powerful tool when used to check tendencies, and gives good treatments of the gamma band and the unstrained ground state for heavy holes. Where more precise treatment is needed the 8×8 $k \cdot p$ model is used.

All simulations are of Zn-face ZnO unless specified otherwise(the only difference between O-face and Zn-face is the reversal of polarization fields)

3.2.1 Quantum Confinement Effects of a Quantum Well

A 1D quantum well for a type I structure has two exciton limits for the ground state transition, i.e (e1-hh1):

- Infinitely thin quantum well(2D limit): $E_{ex,qw} = 4E_{ex}$, $\lambda_{ex,qw} = \lambda_{ex}/2$
- Infinitely thick quantum well (3D bulk exciton limit): $E_{ex,qw} = E_{ex}$, $\lambda_{ex,qw} = \lambda_{ex}$

Between these limits, the exciton correction, which depends on the well width, has to be calculated numerically. This holds true for both the ground state and the excited states, e.g (e1-lh1), (e2-hh2) etc.

Lambda(λ) is defined as the variational parameter which is equivalent to the exciton Bohr radius in units of nm. [27]

In the case of a polar-polar ZnCdO/MgZno SQW structure of identical chemical composition to our experimental samples, i.e $Zn_{0.75}Cd_{0.25}O/Zn_{0.92}Mg_{0.08}O$, varying the well width from 1nm to 10nm with a quantum region encompassing the entire sample and mixed boundary conditions yields figure 3.12

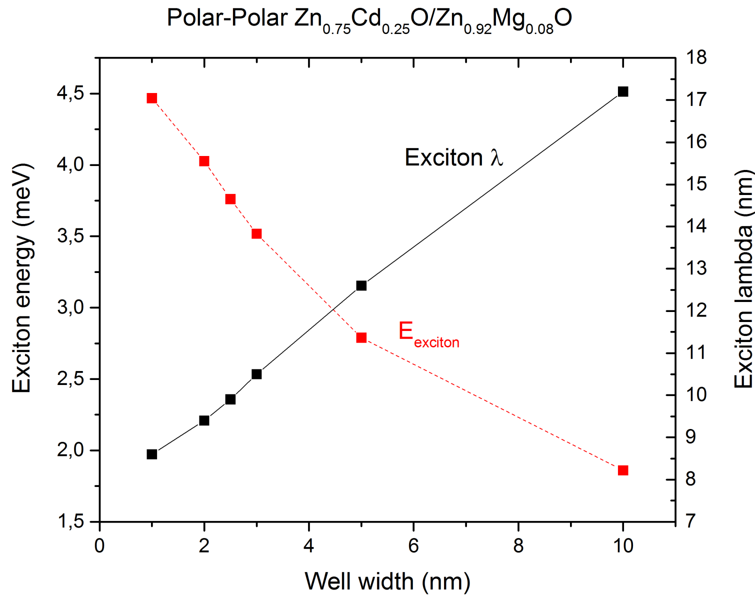

Figure 3.12

The tendencies are as expected, but we note that the values for the exciton binding energies are an order of magnitude smaller than expected bulk value, while the exciton Bohr radius at the same time seem to be exaggerated for increasing well widths. Another method yielding more precise values of the exciton binding energies and the Bohr exciton radius in the quantum well can be found by using Dirichlet boundary conditions and limiting the quantum region to the well, i.e we now view the device as having one ZnCdO SQW with infinite barriers. It is still of interest to investigate the polar case, shown in Fig. 3.13, as it is thought to have a higher probability than the non-polar case of showing any quantum confined Stark effect.

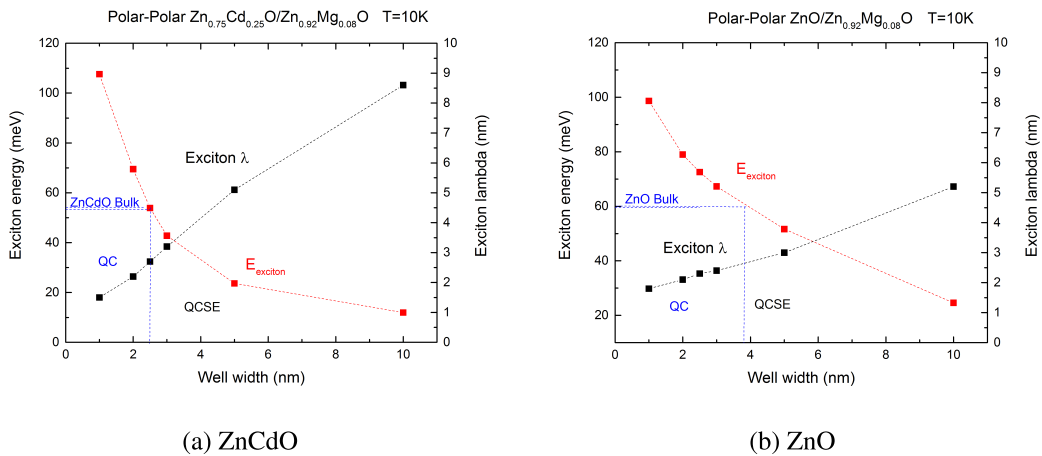

(a) ZnCdO (b) ZnO

Figure 3.13: Exciton binding energy and exciton Bohr radius as a function of well width in polar-polar ZnCdo and ZnO.

The exciton binding energy of 42.77 meV in the 3nm well is in good accordance with the extracted activation energy thought to belong to the exciton binding energy from the equivalent experimental samples. The quantum confined regime is defined by the stippled blue lines, and

is given by the well width L_W corresponding to higher exciton binding energies than expected from bulk value. The QCSE can be explained by the electron-hole separation in the bands induced by the strong fields found in our polar ZnCdO/MgZnO heterostructure.

This can further be illustrated with the oscillator strength, which as we recall from section 2.1.16 is proportional to $|H_{ij}^D|^2$, of the ground state transition (hh1-e1). The spatial separation of electrons and holes in our SQW, as a result of polarization fields, gives us a small $H_{ij}^D|^2$, and thus a small oscillator strength. As previously stated, the effective mass model still holds for ground state transition between the heavy hole and gamma band. In Fig. 3.14 the ground state transition energies and the corresponding overlap matrix is plotted against the well width, L_W.

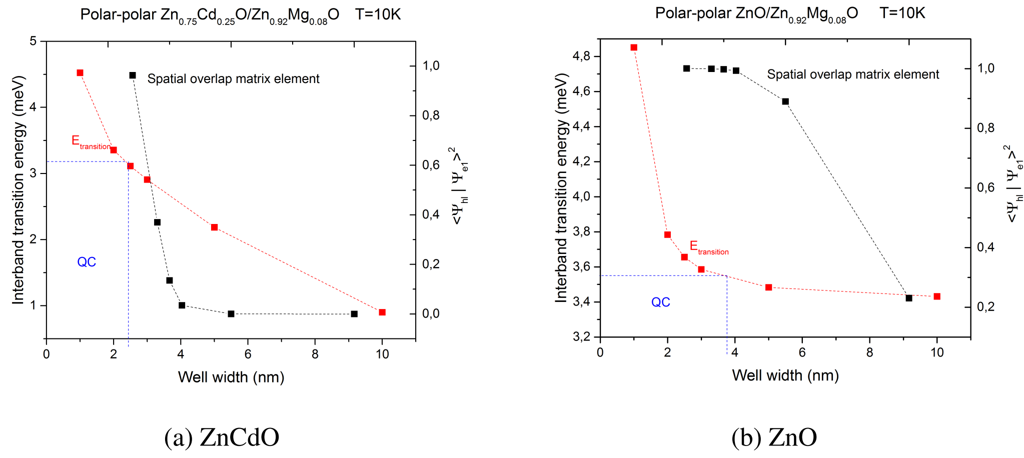

(a) ZnCdO

(b) ZnO

Figure 3.14: Transition energies between the heavy hole band and the gamma band and the corresponding spatial overlap matrix elements as function of well width in polar-polar ZnCdo and ZnO.

The large values for the spatial overlap matrix element, and as a result the oscillator strength, is only found in the already determined quantum confinement regime corresponding to $L_W \sim 2.5nm$ for a polar ZnCdO SQW structure and $L_W \sim 4nm$ for a polar ZnO SQW structure. The difference can be explained by the disparity in polarization fields from the highly polarized $Zn_{0.75}Cd_{0.25}O/Zn_{0.92}Mg_{0.08}O$ SQW, with a calculated electric field along the z-axis of $F = 4022kV/cm$ for $L_{W,ZnCdO} = 3nm$, and the calculated electric field along the z-axis $F = 61kV/cm$ for the corresponding $ZnO/Zn_{0.92}Mg_{0.08}O$ SQW. F matches well with previously reported values for ZnCdO[28].

A closer look at the quantum confined Stark effect

A better visualization of the separation of electron and holes in the QCSE regime can be seen with the placement of the expectation values of holes and electrons in the polar-polar case. As we remember from section 2.3.3, the single-band approximation is not very accurate for holes, and even less so when strain is present. The effective mass model in Fig. 3.15(b) is still doing a good job illustrating the spatial separation of electron and holes in their respective bands as a result of the built-in field, resulting in a lower oscillator strength.

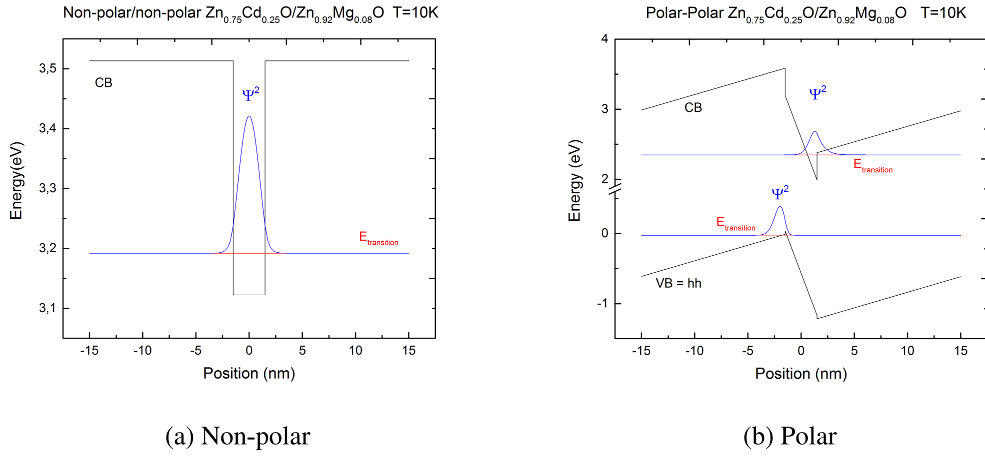

(a) Non-polar (b) Polar

Figure 3.15: Band edges with the expectation values Ψ^2 in the electron/hole ground states in polar and non-polar $Zn_{0.75}Cd_{0.25}O/Zn_{0.92}Mg_{0.08}O$ SQW

Fig. 3.15(a) shows the ground state in a 3nm non-polar ZnCdo/MgZnO SQW with its expectation value found in the middle of the well. As there are no polarization fields to speak of, the spatial overlap matrix element between holes and electrons in their respective ground states is big. No quantum confined Stark effect is expected to be observed in this case.

The following figures show the ground state energy of the 3 nm quantum wells as a function of the applied electric field strength F. The calculated energies can be represented by a parabolic fit. Over the range of electric fields investigated, the ground state energy can be represented by the parabola:

$$E_1(F) = E_1(0) - 0.000365F^2$$

where $E_1(0)$ refers to the ground state energy at zero electric field. Here, the electric field strength, F, is given in units of kV/cm. [29]

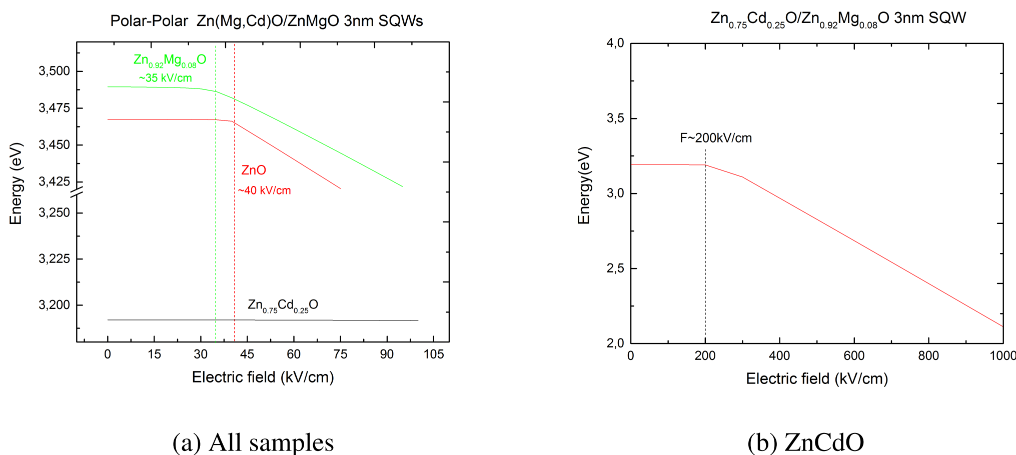

(a) All samples (b) ZnCdO

Figure 3.16: QCSE effects on the energy of the gamma band as a function of electric field strength. Stippled lines indicates the field strength where the QCSE starts to take place.

As one can see from the figures, the ZnMgO/MgZnO and ZnO/MgZnO SQWs are expected to start showing QCSE like behaviour at electric field strengths with values F close to those found

in our calculations. In the case of the ZnCdO/MgZnO SQW it is clearly shown that a stronger electric field is required for our sample to exhibit quantum confined Stark effects, then again the transition regime found at 200kV/cm is an entire order of magnitude lower than the calculated value expected for the $L_{W,ZnCdO} = 3nm$ sample, and the QCSE effects are expected to be more pronounced here than in the other samples, as illustrated in Figs. 3.13-14.

3.2.2 The Extremes

ZnO and CdO form in different stable crystal structures, wurtzite and rock salt respectively, which complicates the fabrication of single-phase alloys in a broad compositional range. [20] Zaoui et al. have predicted rock salt ZnCdO to be more stable than its wurtzite phase for Cd contents $\geq 37.5\%$ based on comparison of corresponding cohesive energies[30]. Other studies report the limit for alloying ZnO with CdO in strict wurtzite phase at 30%Cd[28, 31, 32] As a result of this, it is highly unlikely to achieve a wurtzite CdO/MgZnO QW heterostructure, and a too high Cd concentration can yield unphysical models. In Figs. 3.17-18 we find polar-polar and non-polar band edge models of the theoretical case of a CdO/MgZnO heterostructure with a wurtzite crystal structure.

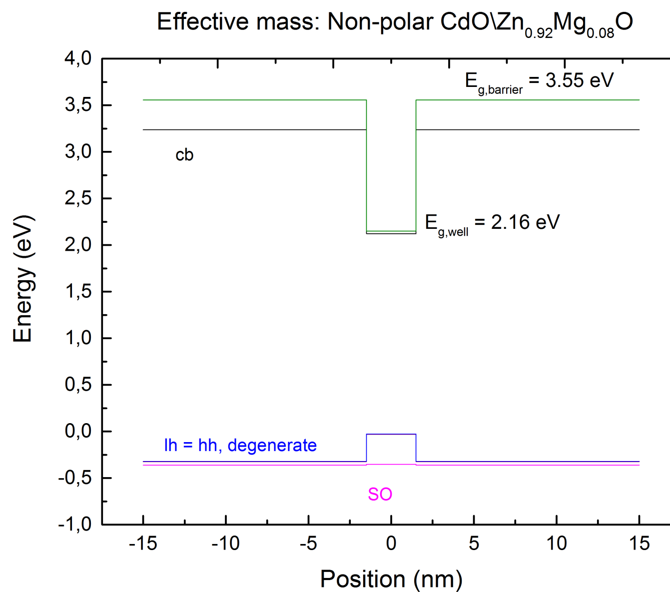

Figure 3.17: Effective mass model of non-polar CdO/$Mg_{0.08}$ZnO band edges.

The bandgap corresponding to the ZnCdO well is found to be slightly lower than reported values of ~2.3 eV at low temperatures. We recall from section 2.3.3 that this might be strain induced. Another reason can be inexact treatment of the valence bands in the effective mass approximation.

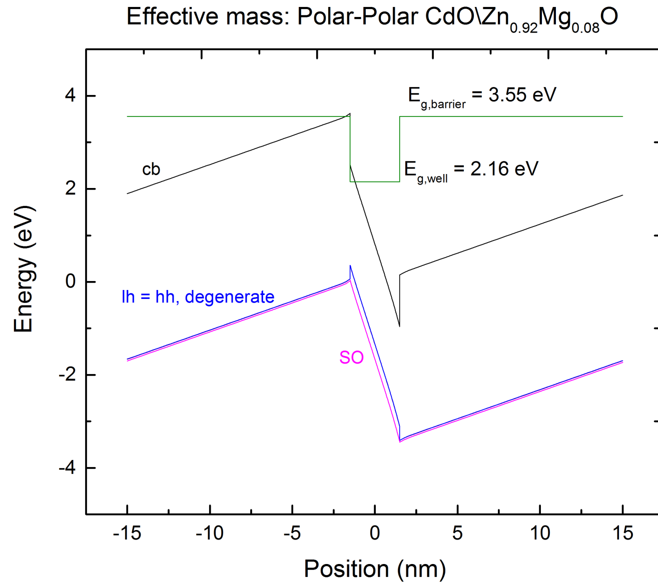

Figure 3.18: Effective mass model of polar-polar CdO/$Mg_{0.08}$ZnO band edges.

As a result of strong polarization fields, the conduction band edge drops beneath the valence band edge at the opposite sides of the SQW. This "broken band edge profile" cannot be solved with the 8×8 $k \cdot p$ model, and a more exact treatment of the valence bands is not possible. In figure 3.19 we can see the piezo and pyroelectric charges for the same system are found at the interfaces between the SQW and barriers, as expected from section 2.3.2. It is shown that piezoelectric effects are dominating at very high Cd concentrations.

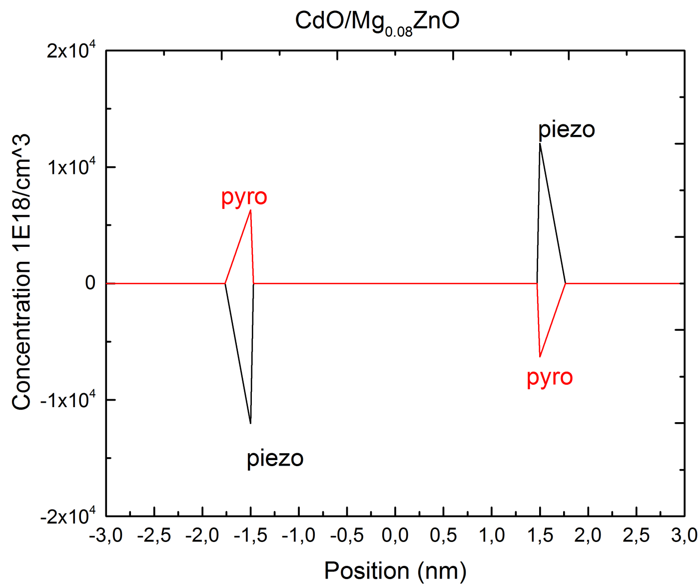

Figure 3.19: Piezo and pyroelectric charges in our CdO/MgZnO SQW model.

The broken band edge profile seems unphysical, and other processes are thought to take place to compensate for the very strong polarization fields found in the polar-polar case. Typically

there are a lot of carriers excited in the quantum wells, and these are able to screen the internal field to some extent, this process is shown in Fig 3.20.

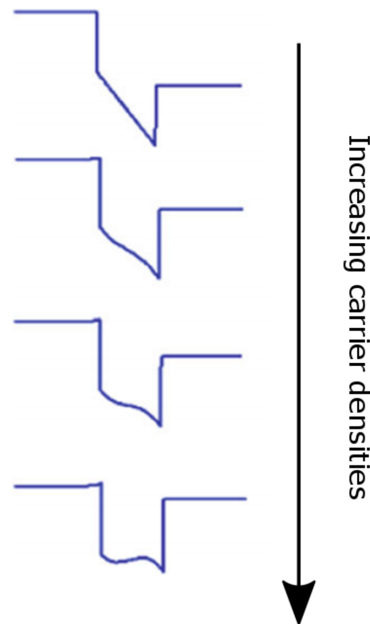

Figure 3.20: Conduction band edge profile varying with increasing carrier densities. Unmodified Fig. can be found in[25]

As a result of this screening, the QCSE is somewhat mitigated, i.e the expected red-shift is reduced and the lifetimes shortened with increasing carrier densities.

Two dimensional electron gas (2DEG) sheet carrier density

High 2DEG sheet carrier densities of the order $10^{13}/cm^2$ have been reported in GaN heterostructures. In fact the wurtzite hexagonal close packed structure with non-centro symmetric property is thought to be the main source for formation of the 2DEG at GaN heterostructure interfaces, mainly due to piezoelectric and pyroelectric polarization. [33, 34]

Equally large internal fields are expected to be present in the theoretical case of high concentration Cd in ZnCdo/MgZnO wurtzite heterostructures. For 90% Cd, the calculated 2DEG sheet

carrier density is found to be $9 \cdot 10^{12}/cm^2$. We reiterate here that such a high Cd concentration in ZnCdO structures is not expected to be found in the wurtzite phase.

Difficulties with the electronic structure in CdO and MgO

CdO and MgO is found to occur in rock salt structure, whereas modest concentrations of $Zn_{1-x}Cd_xO$ and $Zn_{1-x}Mg_xO$ assume the wurtzite structure of the parent compound ZnO. Experimental data for wurtzite CdO and MgO is therefore not available, which complicates the standard approach of deriving the electronic properties of these alloys by interpolation of results for the binary compounds. Janotti and de Walle and Yan et. al [35, 36] report deformation potentials derived from first-principles methods. The problems related to calculations of electronic bandstructure with the local density approximation and density functional theory are well known [37]. Using the deformation potentials derived from these first-principles methods causes problems in the valence band structures, as illustrated in the 8×8 $k \cdot p$ calculation in Fig. 3.21.

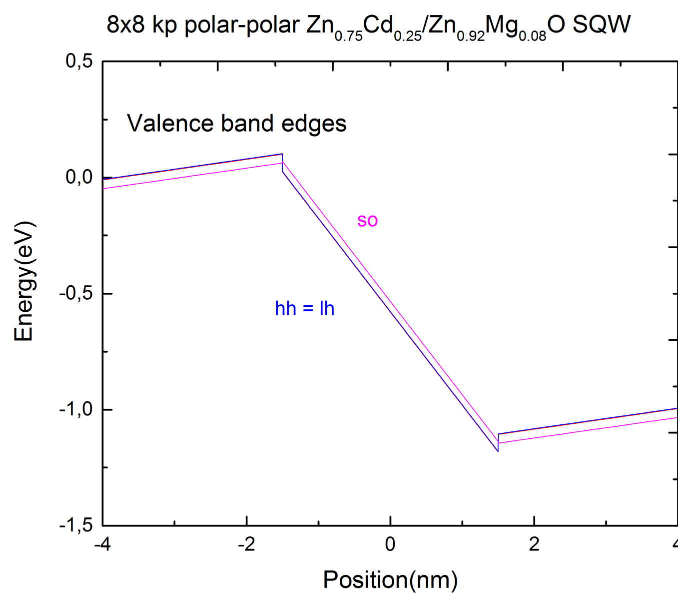

Figure 3.21: Valence band edges using deformation potentials derived from first-principles calculations

As we can see the band edges corresponding to the valence band of the quantum well are inverted, yielding some unphysical system where the well is now serving as a barrier for holes in the valence band.

By systematically changing the deformation potentials, while keeping a steady relationship between them as according to the first-principle calculations, it is possible to get a more physical representation of the ZnCdO system than given in Fig. 3.21. The quasicubic approximation used for determining the deformation potentials in GaN[38] was also attempted, but it does indeed

seem to break down for wz-CdO as reported by Yan et al.[36], as it does not appear to result in a type I QW.

The deformation potentials in the quasicubic approximation are given as:

$$D_1 + D_3 = D_2,$$

$$D_3 + 2D_4 = 0,$$
$$D_3 + 4D_5 = \sqrt{2}D_6.$$

A comparison with reported calculations for ZnO/MgZnO and ZnCdO/MgZnO was conducted to assess the material parameters and polarization fields using the single-band envelope function approximation. The stippled lines are the self-consistent SC band structures obtained by solving the Schrödinger equation for electrons and the 3×3 Hamiltonian for holes as reported by Jeon et al.[39]

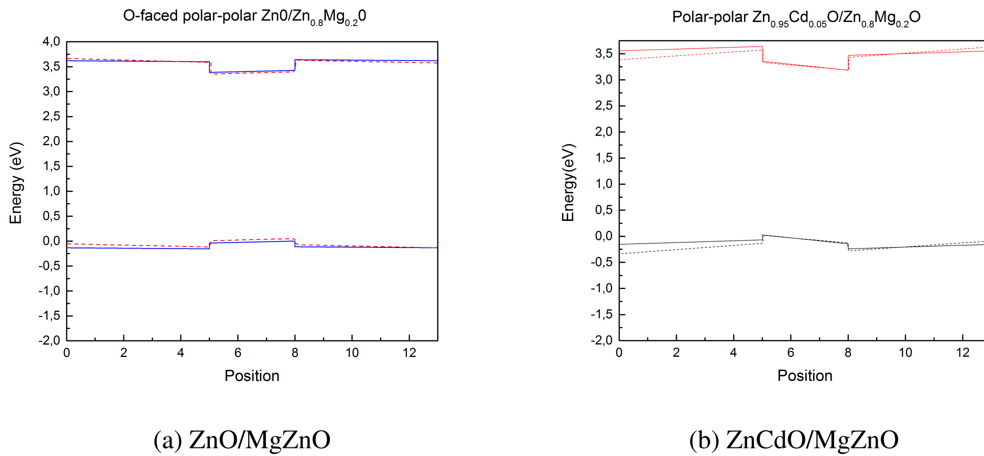

(a) ZnO/MgZnO (b) ZnCdO/MgZnO

Figure 3.22: A comparison between the effective mass approximation and reported calculations

To get corresponding band edges in the ZnO/MgZnO, the initial values for the spontaneous polarization constants in Mgo and ZnO, reported by Gopal and Spaldin [40], was only changed with 3%. The spontaneous polarization(pyroelectric polarization) is the dominating factor in the ZnO/$Zn_{0.8}Mg_{0.2}O$ heterostructure, as can be seen in Fig. 3.22.

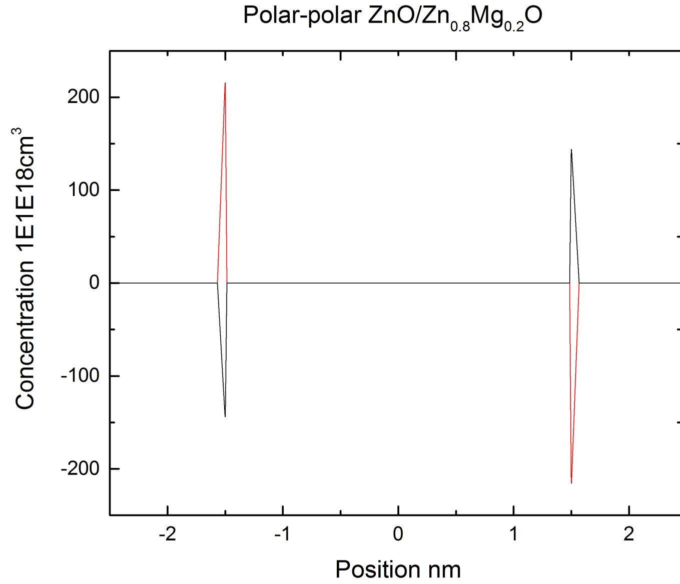

Figure 3.23: Polarization fields in ZnO/MgZnO

In the case of ZnCdO it is a bit more complicated, and the piezoelectric constants carry more weight. A polarization field giving the same incline of the band edges in the quantum well does end up giving a different slope in the barriers, meaning that the polarization fields in these areas are treated differently. This difference can be explained by some undefined interface/surface states at the end of their model, or that the two approaches yield different polarization fields.

3.2.3 Coupling in MQWs

As mentioned in section 2.3.3 a thorough study of the valence band edges cannot be done using the effective mass model. Tendencies shown in MQW models, with regards to coupled wells, will therefore be restricted to the conduction band in the following section.

The bandgap of $Zn_{1-x}Mg_xO$ is given by $3.37+2.51x$ eV, the value of x is limited to 0.43[25, 41]. Thus, a Mg concentration of 8%, will yield a bandgap of 3.57 eV, this is in good accordance with our theoretical values shown in Figs. 3.17-18. The Mg concentration dependency of the bandgap means that it is possible to adjust barrier heights with varying the Mg concentration in our barriers.

Tunneling between barriers depend on both barrier width and height. Therefore it can be argued that the best contenders among our experimental samples for showing coupling between quantum wells, are the $ZnO/Zn_{0.92}Mg_{0.08}O$ and $Zn_{0.97}Mg_{0.03}O/Zn_{0.92}Mg_{0.08}O$ 3nm MQWs / 10 nm barriers. In Fig. 3.24 the coupling of wells in the gamma band edge is shown for the first quantized electron state with decreasing barrier height in the ZnO/MgZnO MQW system.

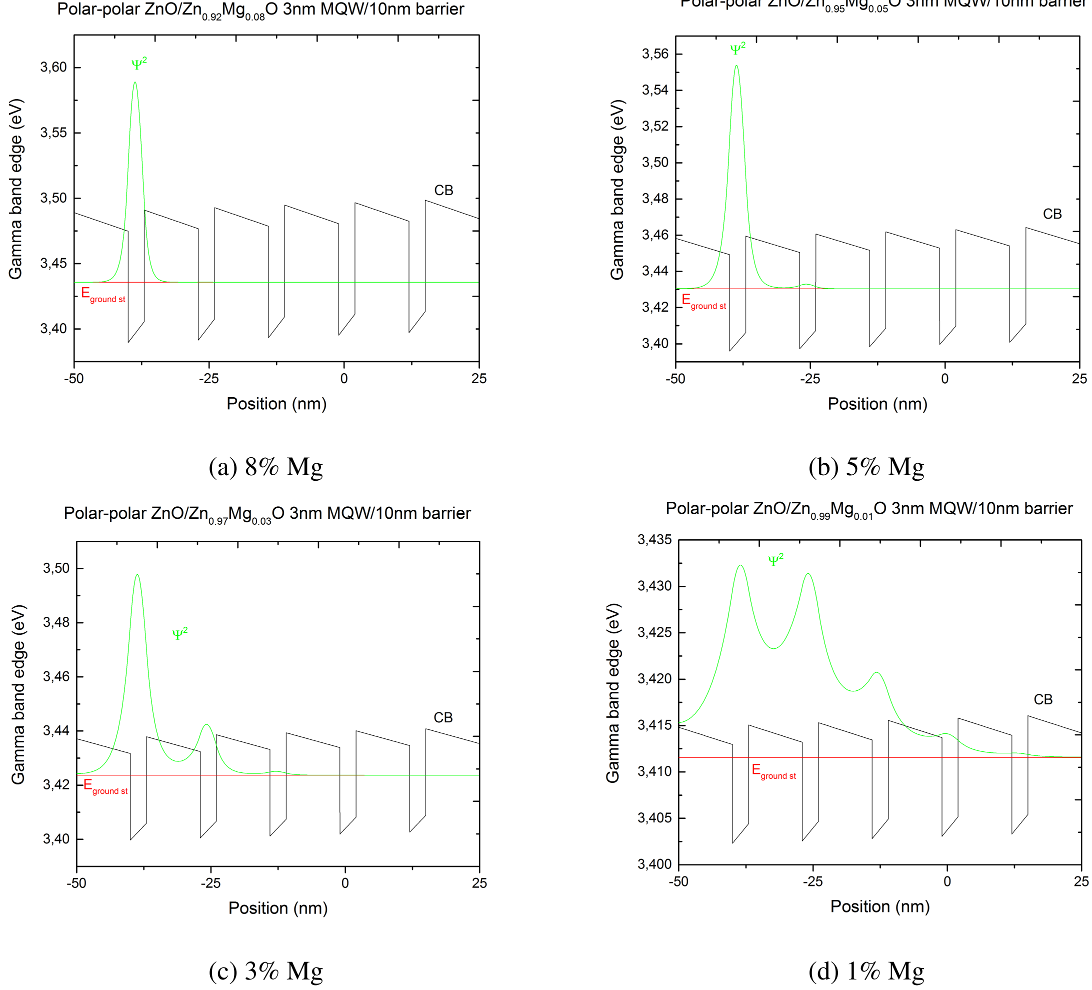

(a) 8% Mg

(b) 5% Mg

(c) 3% Mg

(d) 1% Mg

Figure 3.24: Gamma band edges and the expectation value Ψ^2 for the first quantized electron state with varying Mg concentrations.

The coupling between wells is seen to increase with decreasing barrier height. At 8% the wavefunction decreases exponentially in the barrier, and there is no communication between the wells, while at 5% there is a small wavefunction overlap between two adjacent wells. For 3% Mg concentration this coupling is more pronounced, and one more well is included in the overlap. The coupling effects for 1% Mg in the barrier are seen to be very strong for nearby wells, and as many as ten at a time are, to different degrees, expected to show coupled behaviour.

The increase in tunnelling through the barriers can be viewed in the context of the position-momentum uncertainty discussed in section 2.1.7. Decreasing the Mg content of our barriers is shown to lower the bandgap, and thus the barrier height

$$V_m \sim (E_{g,barrier} - E_{g,well}).$$

In the case of the ZnO/MgZnO MQW system, the Mg concentration limit for coupled wells is found to be at 8%, and we do not expect to see any communication between quantum wells at higher concentrations. Following the determination of bandgaps in ZnMgO, we find that

the barrier height in our ZnMgO/MgZnO experimental heterostructure is comparable to that of the 5% Mg content model. The minimal communication shown for 5% Mg indicates that no coupling behaviour is likely to occur for any of our experimental samples. To show that the barrier width also plays a part in the coupling of wells, the ZnO/$Zn_{0.92}Mg_{0.08}O$ MQW was calculated with 10/7/5/3 nm barriers as shown in Fig. 3.25.

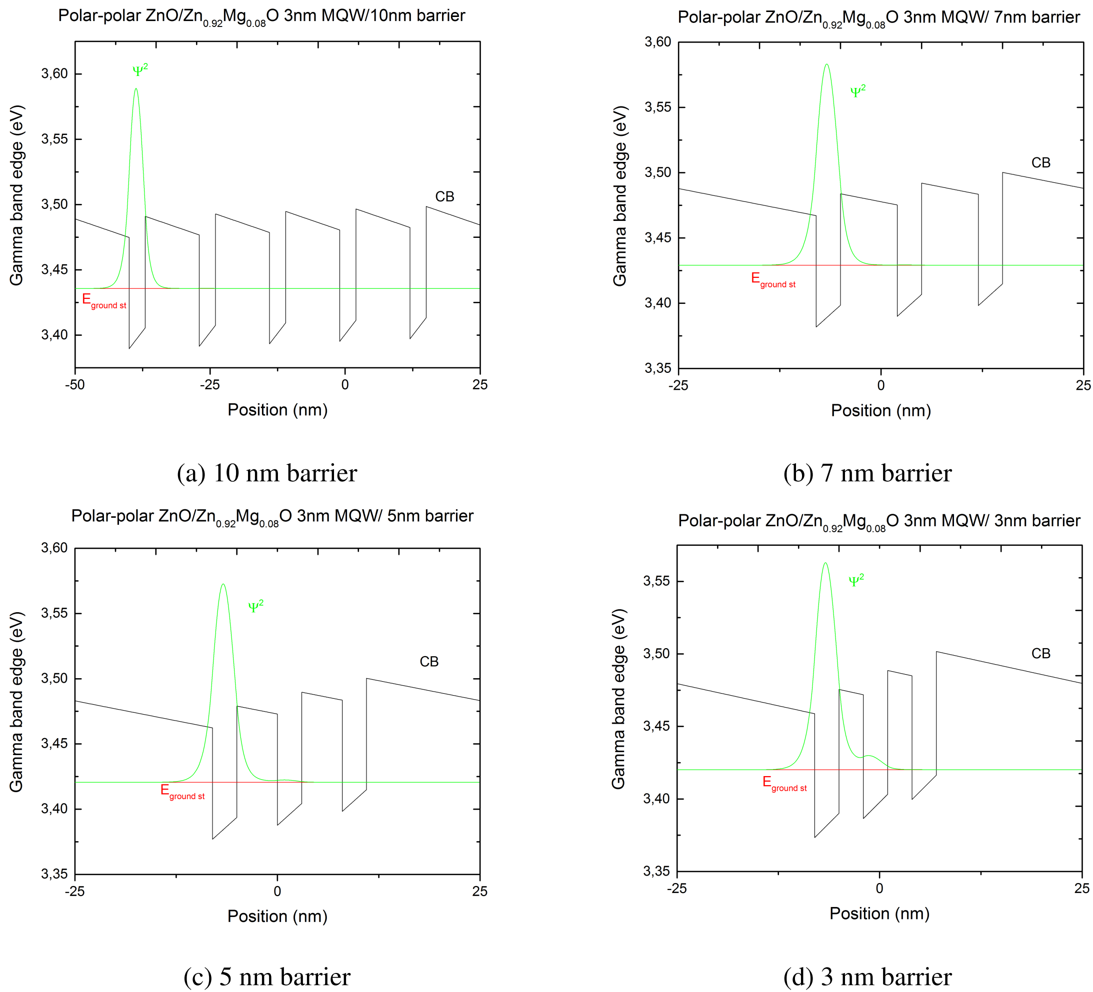

(a) 10 nm barrier

(b) 7 nm barrier

(c) 5 nm barrier

(d) 3 nm barrier

Figure 3.25: Gamma band edges and the expectation value Ψ^2 for the first quantized electron state with varying well widths.

The only noticeable communication between quantum wells is found for the case where barrier width is equal to that of the quantum wells. Varying both the barrier height and width can be useful tools for achieving coupling between wells, and in some cases even a superlattice. Even though we don't seem to have superlattice behaviour or coupling in our experimental samples based on these theoretical models, an increase in PL yield is expected in MQW heterostructures compared to SQWs.

According to Zippel et al. [42] a study using time resolved photoluminescence on a series of coupled QWs, revealed a clear two-component decay for barrier widths of 2.2, 4 and 6 nm. The additional decay component was attributed to a spatially indirect exciton, which only occurs when the wells are coupled. This doesn't seem to be physical in the case of coupling between

identical quantum wells. Davis and Jagadish[25] suggest that the additional decay component arises from recombination between symmetric electron and antisymmetric hole or vice versa. Control of the optical properties of Zn(Mg,Cd)O quantum wells can be achieved by varying the structure and chemical composition. The case of spatially indirect excitons can be realised with coupling between asymmetric wells, where the lifetimes are expected to increase, and as a result reducing the oscillator strength. These properties have been thoroughly discussed throughout the work, and a study of said properties using quantum mechanical modelling and time resolved photoluminescence in conjunction can therefore be expected to give a good insight to what is actually happening in the case of coupling between wells and possible superlattices.

Chapter 4

Summary and Concluding Remarks

4.1 Summary

The study set out to investigate the importance of alloy composition, structuring of Zn(Mg,Cd)O heterostructures and the related polarization fields to quantum confinement effects (including a closer look at the quantum confined Stark effect), recombination mechanisms and coupling of wells in MQW structures. Photoluminescence spectroscopy in conjunction with single- and multi-band envelope approximation functions within the confines of $k \cdot p$ perturbation theory and $next$**nano**^{3} software was used to provide insight on the underlying mechanisms of quantum confinement effects and recombination.

Evidence derived from $k \cdot p$ perturbation theory was presented showing the dependence of quantum confinement effects on well width. The quantum confinement regime was defined to the area where the quantum wells were thin enough to exert exciton binding energies far above the expected bulk value, likewise was the QCSE regime found for increasing well widths where the exciton binding energy dropped below the bulk value. A closer look was taken at the quantum confined Stark effects, and the electron-hole separation as a result of polarization fields was found and illustrated in the context of a polar-polar SQW heterostructure. The polarization fields were identified and shown to occur at the interfaces, as was expected from previous theory. Lifetimes and oscillator strengths were defined and treated with respect to the quantum confinement effects. The QC and QCSE regimes and effects were well defined, not only with respect to exciton binding energies, but also with oscillator strengths and radiative lifetimes in our Zn(Mg,Cd)O heterostructure systems, making for possible comparisons with time resolved photoluminescence spectroscopy measurements.

Activation energies from our Zn(Mg,Cd)O heterostructures were extracted using time-integrated and time resolved photoluminescence spectroscopy, and some likely contenders for the extracted values were identified. One of these was the activation energy thought to correspond to the exciton binding energy in our $Zn_{0.75}Cd_{0.25}O$ 3nm QW, whose value of 42 meV was reproduced in an independent effective mass approximation model of calculated exciton binding energies as a function of well width in an analogous semiconductor system. Time resolved photoluminescence spectroscopy was further utilized to identify and separate radiate and non-

radiative lifetimes, which in turn gave another indication on the nature of quantum confined Stark effects. The differences between the polar and non-polar heterostructures were discussed with repect to lifetimes, and the QCSE was identified in the polar sample. A detailed view of lifetimes as a function of temperature was given, and the differences in thermal quenching between the polar and the non-polar sample was established.

The possibility of achieving coupled quantum wells in the Zn(Mg,Cd)O heterostructures was investigated using the effective mass approximation, and the most likely contenders for showing communication between adjacent wells in our experimental samples were identified as the ZnMgO/MgZnO MQWs. The dependency of coupling between quantum wells on barrier width and height was discussed, it was further shown that both altering the barrier height by varying Mg concentrations, and varying barrier widths are viable ways of controlling communication between wells.

The limiting cases of the different $k \cdot p$ perturbation models were found in the case of high Cd content Zn(Mg,Cd)O wurtzite heterostructures, especially in treatment of the valence band. Both due to the spherical mass tensor not being a good approximation to the hexagonal wurtzite structure, and because of the poorly defined material parameters of wurtzite CdO found in litterature. Only first-principle deformation potentials have previously been found for CdO in wurtzite phase, which are not necessarily exact as a result of the well known bandgap problem existing in LDA and DFT. An approach using the quasicubic approximation, which gives the deformation potentials in GaN, was attempted and discarded as it didn't result in any known QW structure. The deformation potentials were therefore systematically changed, loosely maintaining the relationship previously reported by first-principles calculations, until the $k{\cdot}p$ calculations yielded a result that was of physical nature.

4.2 Concluding Remarks

Photoluminescence spectroscopy and $k \cdot p$ perturbation theory have been shown to be powerful tools that may facilitate the correlation of the performance of Zn(Mg,Cd)O heterostructures to their processing.

Varying barrier height and width in MQWs can be a way of realizing superlattices in Zn(Mg,Cd)O MQW heterostructures, giving another way of manipulating the optical properties of the system. Moreover it has been shown that $k \cdot p$ perturbation theory can be used to find heterostructures likely to exhibit coupled behaviour, which in turn can be studied experimentally. One promising experimental approach is time resolved photoluminescence spectroscopy, a method that has proven to be effective in characterizing decay components and lifetimes. The importance of lifetimes and oscillator strengths in the quantum confinement and quantum confined Stark effect regimes, makes the use of these theoretical and experimental approaches in conjunction a very powerful tool to understand the underlying mechanisms.

The single- and multi-band envelope function approximations have proven to be extremely effective in treating well defined semiconductor systems. The limitations are encountered when dealing with unknown systems and poorly defined material parameters; these limitations can be

approached with a careful modification to the parameters. In combination with other theoretical studies and experimental data, the $k \cdot p$ perturbation treatment can be used as a tool to attack difficult problems yielded by challenging systems. It is therefore important to note that this method is not a black box tool in the framework of $next\mathbf{nano}^3$, but requires a good knowledge of semiconductor and quantum physics to be used reliably.

4.3 Future Work and Potential Applications

There are many interesting aspects of applying $k \cdot p$ perturbation theory to treat our systems quantum mechanically, and the different uses go far beyond what has been looked at in this study. A quick summary of elements that would be of interest with regards to our Zn(Mg,Cd)O heterostructures include, but are not limited to:

- Look at $k \cdot p$ dispersion of our theoretical models.
  - Identify minibands and DOS in potential superlattices.
- Take a closer look at intersubband transitions in quantum wells.
- Include surface states and their effects on the bending of band edge profiles.
- Include doping and study the effects with respect to modelling.
- Look into the effects of varying dimensionality of quantum structures.
- Further study of physical consequences of varying temperature in the theoretical models.

A more detailed study of coupling between wells in Zn(Mg,Cd)O MQW heterostructures, utilizing both time resolved photoluminescence spectroscopy and quantum mechanical modelling in the context of $k \cdot p$ perturbation theory, should be conducted. This may lead to an increased understanding of yet another way of manipulating optical properties in promising MQW heterostructures.

Bibliography

[1] J. Browne, “Proposal - the energy crisis and climate change,” 2016.

[2] H. Morkoç and Ümit Özgur, *Zinc Oxide: Fundamentals, Materials and Device Technology*. WILEY-VCH, 2009.

[3] D. Look, *Recent advances in ZnO materials and devices*. 2001.

[4] N. H. Nikel and E. Terukov, *Zinc oxide – a material for micro- and optoelectronic applications*. 2005.

[5] S. Pearton, *GaN and ZnO-based Materials and Devices*. 2012.

[6] S. Baruah, *ZnO Nanostructures for Alternate Energy Generation*. 2015.

[7] B. G. Streetman and S. K. Banerjee, *Solid State Electronic Devices Sixth Edition*. 2006.

[8] T. Zibold, *Semiconductor based quantum information devices: Theory and simulations*. PhD thesis, Technische Universität München, 2007.

[9] P. Hofmann, *Solid State Physics*. WILEY-VCH, 2012.

[10] T. Nordby, *Defects and transport in crystalline solids*. 2015.

[11] S. A. Campbell, *Fabrication Engineering at the micro- and nanoscale 4th edition*. 2013.

[12] D. J. Griffiths, *Introduction to Quantum Mechanics, 2nd edition*. Pearson, 2004.

[13] I. Pelant and J. Valenta, *Luminescence Spectroscopy of Semiconductors*. 2012.

[14] C. F. Klingshirn, *Semicoductor Optics 4th Edition*. 2012.

[15] M. Razavy, *Quantum theory of tunneling 2nd Edition*. 2014.

[16] M. Dyakonov, “Basics of semicoductor and spin physics,” 2008.

[17] T. H. Gfroerer, “Photoluminescence in analysis of surfaces and interfaces,” 2006.

[18] S. Birner, *Modeling of semiconductor nanostructures and semiconductor-electrolyte interfaces*. PhD thesis, Technischen Universität München, 2011.

[19] S. Birner, “Basics 1,” 2006.

[20] V. Venkatachalapathy, A. Galeckas, M. Trunk, T. Zhang, A. Azarow, and A. Kuznetsov, “Understanding phase separation in zncdo by a combination of structural and optical analysis,” 2011.

[21] W. Yang, L. Wong, S. J. Wang, H. D. Sun, C. H. Ge, A. Y. S. Lee, and H. Gong, "Photoluminescence characteristics of zncdo/zno single quantum well grown by pulsed laser deposition," 2011.

[22] T. Guillet, T. Bretagnon, T. Taliercio, P. Lefebvre, B. Gil, C. Morhain, and X. Tang, "Time-resolved spectroscopy of exexciton transitions in zno/(zn, mgo) quantum wells," 2007.

[23] V. A. Fonoberov, K. A. Alim, and A. A. Balandin, "Photoluminescence investigation of the carrier recombination processes in zno quantum dots and nanocrystals," 2006.

[24] M. Gurioli, A. Vinattieri, M. Colocci, C. Deparis, J. Massies, G. Neu, A. Bosacchi, and S. Franchi, "Temperature dependence of ther radiative and nonradiative recombination time in gaas/alxga1-xas quantum-well structures," 1991.

[25] J. D. . C. Jagadish, "Chapter 14 zno/mgzno quantum wells," 2012.

[26] G. W. Drake, *Precision Oscillator Strength and Lifetime Measurements*. 2006.

[27] S. Birner, "1d exciton in qw," 2016.

[28] S. Kalusniak, S. Sadofev, J. Puls, H. J. Wünsche, and F. Henneberger, "Polarization fields in (zn,cd)ozno quantum well structures," 2007.

[29] S. Birner, "Quantum confined stark effect (qcse)," 2016.

[30] A. Zaouia, M. Zaouia, S. Kacimia, A. Boukorttb, and B. Bouhafsa, "Stability and electronic properties of znxcdd1-xo alloys," 2009.

[31] S. Shigemori, A. Nakamure, J. Ishihara, T. Aoki, and J. Temmyo 2004.

[32] S. Sadofev, P. Schäfer, S. Blumstengel, and F. Henneberger 2007.

[33] S. Baskaran, A. Mohanbabu, N. Anbuselvan, N. Mohankumar, D. Godwinraj, and C. Sarkar, "Modeling of 2deg sheet carrier density and dc characteristics in spacer based algan/aln/gan hemt devices," 2013.

[34] J. Piprek, *Nitride Semiconductor Devices Principles and Simulation, WILEY-VCH Verlag GmbH & Co*. 2007.

[35] A. Janotti and C. G. V. de Walle, "Absolute deformation potentials and band alignment of wurtzite zno, mgo, and cdo," 2007.

[36] Q. Yan, P. RInke, omme Winkelnkemper, A. Qteish, and D. Bimberg, "Strain eeffect and band parameters in mgo, zno and cdo," 2012.

[37] I. N. Yakovin and P. Dowben, "The problem of the band gap in lda calculations," 2007.

[38] Q. Yan, P. Rinke, M. Scheffler, and C. G. V. de Walle 2009.

[39] H. C. Jeon, S. H. Park, S. J. Lee, T. W. Kang, and T. F. George, "Electronic and optical properties of cdzno quantum well structures with electric field and polarization effects," 2010.

[40] P. Gopal and N. Spaldin 2006.

[41] V. Coleman and C. Jagadish, *Basic properties and applications of ZnO.* 2006.

[42] J. Zippel, M. Stolzel, G. Benndorf, M. Lorenz, H. Hochmuth, and M. Grundmann 2010.